

1

2

3

4

# Cosmic ray validation of electrode positions in small-strip thin gap chambers for the upgrade of the ATLAS detector

5

Lia Formenti

6

7

8

Department of Physics  
McGill University, Montreal  
October, 2021

9

10

11

12

13

A thesis submitted to  
McGill University  
in partial fulfillment of the  
requirements of the degree of  
Master of Science

# <sup>15</sup> Table of Contents

<sup>16</sup>	<b>1</b>	<b>Introduction</b>	<b>1</b>
<sup>17</sup>	<b>2</b>	<b>High energy particle physics</b>	<b>4</b>
<sup>18</sup>	2.1	The Standard Model . . . . .	4
<sup>19</sup>	2.2	Beyond the Standard Model . . . . .	6
<sup>20</sup>	2.3	Studying high energy particle physics with accelerators . . . . .	7
<sup>21</sup>	<b>3</b>	<b>The LHC and the ATLAS experiment</b>	<b>9</b>
<sup>22</sup>	3.1	The Large Hadron Collider . . . . .	9
<sup>23</sup>	3.2	The High-Luminosity LHC . . . . .	10
<sup>24</sup>	3.3	The ATLAS experiment . . . . .	12
<sup>25</sup>	<b>4</b>	<b>The New Small Wheels</b>	<b>17</b>
<sup>26</sup>	4.1	Motivation for the New Small Wheels . . . . .	17
<sup>27</sup>	4.2	Design of the NSWs . . . . .	20
<sup>28</sup>	4.3	Small-strip thin gap chambers . . . . .	20
<sup>29</sup>	4.4	sTGC Quadruplet Construction . . . . .	23
<sup>30</sup>	4.5	NSW alignment . . . . .	24
<sup>31</sup>	<b>5</b>	<b>Using cosmic muons to measure relative strip position offsets</b>	<b>27</b>
<sup>32</sup>	5.1	Cosmic rays . . . . .	27
<sup>33</sup>	5.2	Experimental setup . . . . .	28

34	5.3 Data acquisition . . . . .	29
35	5.4 Data preparation . . . . .	30
36	5.4.1 Data quality cuts on electrode hits . . . . .	30
37	5.4.2 Clustering and tracking . . . . .	30
38	5.5 Relative local offsets . . . . .	32
39	5.6 Systematic uncertainty . . . . .	38
40	5.7 Discussion . . . . .	39
41	<b>6 Using x-rays to measure relative strip position offsets</b>	<b>41</b>
42	6.1 Experimental setup . . . . .	41
43	6.2 Data acquisition . . . . .	43
44	6.3 Data preparation . . . . .	43
45	6.4 Measuring local offsets . . . . .	43
46	6.5 Measuring relative local offsets . . . . .	45
47	<b>7 Comparing cosmic muon and x-ray relative strip position offsets</b>	<b>48</b>
48	7.1 Results . . . . .	48
49	7.2 Discussion . . . . .	53
50	<b>8 Outlook and summary</b>	<b>55</b>
51	8.1 Outlook . . . . .	55
52	8.2 Summary . . . . .	56
53	<b>References</b>	<b>57</b>
54	<b>APPENDICES</b>	<b>64</b>
55	<b>A Cluster position uncertainty</b>	<b>65</b>
56	<b>B Analysis statistics</b>	<b>67</b>

57	<b>C Analysis systematics</b>	<b>69</b>
58	C.1 Residual distribution fit function	69
59	C.2 Cosmic muon data collection voltage	72
60	C.3 Cluster fit algorithm	73
61	C.4 Differential non-linearity	74
62	<b>D Printable plots</b>	<b>77</b>

## Abstract

64 The Large Hadron Collider (LHC) is used to generate subatomic physics processes at the  
65 energy frontier to challenge our understanding of the Standard Model of particle physics.  
66 The particle collision rate at the LHC will be increased up to seven times its design value in  
67 2025-2027 by an extensive upgrade program. The innermost endcaps of the ATLAS muon  
68 spectrometer consist of two wheels of muon detectors that must be replaced to maintain  
69 the muon momentum resolution in the high-rate environment. The so-called New Small  
70 Wheels (NSWs) are made of two detector technologies: micromegas and small-strip thin gap  
71 chambers (sTGCs). The sTGCs are gas ionization chambers that hold a thin volume of gas  
72 between two cathode boards. One board is segmented into copper readout strips of 3.2 mm  
73 pitch that are used to precisely reconstruct the coordinate of a passing muon. Modules of  
74 four sTGCs glued together into quadruplets cover the NSWs. Quadruplets were designed  
75 to achieve a 1 mrad angular resolution to fulfill the spectrometer's triggering and precision  
76 tracking requirements. To achieve the required angular resolution the absolute position of  
77 the readout strips must be known in the ATLAS coordinate system to within 100  $\mu\text{m}$ . At  
78 McGill University, the performance of sTGC quadruplets was characterized using cosmic ray  
79 data before being sent to CERN, where the charge profile left by x-rays is used to measure  
80 the offset of the strip patterns with respect to nominal at a limited number of points on  
81 the surface of each quadruplet. The x-ray strip position measurements have acceptable but  
82 limited precision and do not span the whole area of the strip layers. Given the importance of  
83 knowing the absolute position of each readout strip to achieve the performance requirements  
84 of the NSWs, the x-ray method must be validated by an independent method. Cosmic ray  
85 data is used to characterize the relative alignment between layers and validate the x-ray  
86 method.

## Résumé

Le grand collisionneur des hadrons (LHC) utilise des collisions de protons afin de générer des processus de la physique subatomique à la frontière même de la haute énergie, et ceci afin de tenter remettre en cause le modèle standard de la physique des particules. Le taux des collisions entre protons au LHC sera augmenté jusqu'à sept fois le taux nominal d'ici 2025-2027 à l'aide d'un programme de mise à niveau de grande envergure. Une partie du spectromètre à muons du détecteur ATLAS consistant de deux roues de détecteurs de muons doit être remplacée afin de maintenir la résolution sur l'inertie des muons à haut taux de collision. Appelées les Nouvelles Petites Roues (NSWs), elles utilisent deux technologies de détection différentes: des chambres micromegas et des chambres à petites bandes et à intervalles fins (sTGCs). Les sTGCs sont des chambres d'ionisation de gaz, qui contiennent un volume très fin de gaz entre deux panneaux cathodiques. Un panneau est segmenté avec de petites bandes en cuivre en pente de 3.2 mm. Ceux-ci détectent le signal laissé par des muons et permettent la mesure précise des coordonnées spatiales des muons qui traversent le détecteur. Des modules de quatre sTGCs collés ensemble en quaduplets couvrent la superficie des NSWs. Ces quadruplets ont été conçus afin de permettre une résolution angulaire de 1 mrad, et de satisfaire les exigences des systèmes de déclenchement et de mesures de précision. Afin d'atteindre cette résolution angulaire il faut que la position absolue de chaque bande soit connue au sein du détecteur ATLAS avec une précision d'au moins 100  $\mu$ m. À l'Université de McGill, la performance des quadruplets a été caractériser avec des rayons cosmiques avant leur envoi au CERN, où le profil des charges laissé par des rayons X est utilisé pour mesurer le déplacement du motif des bandes par rapport à leur emplacement nominal. Ceci est fait à un nombre de positions limité sur la surface des quadruplets. Ces déplacements, mesurés par les rayons X, ont une précision acceptable mais limitée et ne couvrent pas la région entière des panneaux. Étant donné l'importance de la caractérisation précise de la position absolue de chaque bande afin de réaliser les exigences de rendement des NSWs, une méthode indépendante de validation de la méthode des rayons X est requise. Les données recueillies avec les rayons cosmiques sont utilisées pour caractériser l'alignement relatif entre les panneaux et valider la méthode des rayons-X.

## Acknowledgements

- 117 Experimental particle physics projects are never done alone. I am grateful to have been  
118 working with the ATLAS Collaboration for two years now.
- 119 Thank you to Dr. Brigitte Vachon for her guidance throughout this project and for editing  
120 this thesis. I am consistently amazed by her ability to jump into the details of my project  
121 and discuss them with me.
- 122 Thanks also to Dr. Benoit Lefebvre, who collected some of the data used in this thesis, wrote  
123 several software tools I used to analyze the data and advised me several times throughout  
124 this project.
- 125 Thank you to my labmates at McGill University, Dr. Tony Kwan, Kathrin Brunner, John  
126 McGowan and Charlie Chen. Kathrin taught me mechanical skills that I will apply elsewhere.  
127 Tony, manager of the laboratory, created the most encouraging, trusting and productive work  
128 environment I have ever been apart of.
- 129 Thank you to the friends I can call on at anytime, and thank you to my family whose  
130 constant support makes every step possible.

## Contribution of authors

I, the author, was involved in collecting the cosmic ray data from September 2019 - March 2021. I did not design the cosmic ray testing procedure nor write the data preparation software, but I participated in using the software to analyze cosmic ray results. In the thesis, the terms “clustering,” “local offset” and “relative local offset” are defined. Cosmic ray clustering was done in the data preparation software, but I redid the fit afterwards to explore sensitivity to the fit algorithm. With help from Dr. Lefebvre and Dr. Vachon, I helped design the software that calculated the relative local offsets from cosmic ray data. I wrote that software on my own. I was not involved in the design, data collection, data preparation or analysis of the x-ray data. I also was not involved in creating an alignment model from the x-ray data. I used the x-ray local offsets calculated using x-ray data analysis software to calculate relative local offsets with x-rays. I did the comparison between the x-ray and cosmic ray data.

I hereby declare that I am the sole author of this thesis. This is a true copy of the thesis, including any required final revisions, as accepted by my examiners.

<sup>146</sup>

# Chapter 1

<sup>147</sup>

## Introduction

<sup>148</sup> The Standard Model (SM) is a theoretical framework that describes experimental observa-  
<sup>149</sup> tions of particles and their interactions at the smallest distance scales; however, the questions  
<sup>150</sup> the SM does not address motivate more experimentation.

<sup>151</sup> Accelerators collide particles to generate interactions that can be recorded by detectors  
<sup>152</sup> for further study. Detectors measure the trajectory and energy of all secondary particles  
<sup>153</sup> produced in collisions to understand the interaction. The Large Hadron Collider (LHC) [1]  
<sup>154</sup> at CERN is the world’s most energetic particle accelerator. Its energy makes it a unique  
<sup>155</sup> tool to study elementary particles and their interactions in an environment with conditions  
<sup>156</sup> similar to what would have existed in the early universe. If study at the energy frontier is  
<sup>157</sup> to continue, the LHC must go on.

<sup>158</sup> After 2025, the statistical gain in running the LHC further without significant increase in  
<sup>159</sup> beam intensity will become marginal. The High Luminosity Large Hadron Collider (HL-  
<sup>160</sup> LHC) project [2] is a series of upgrades to LHC infrastructure that will allow the LHC  
<sup>161</sup> to collect approximately ten times more data than in the initial design by  $\sim$ 2030. The  
<sup>162</sup> increase in LHC beam intensity will result in a large increase in collision rate that will make  
<sup>163</sup> accessible and improve statistics on several measurements of interest [3], many only possible  
<sup>164</sup> at the LHC and the energy frontier. The increase in beam intensity will also increase the  
<sup>165</sup> level of background radiation, requiring major upgrades to the experiments used to record  
<sup>166</sup> the outcomes of the particle collisions.

<sup>167</sup> The ATLAS experiment [4] is one of the LHC’s general-purpose particle detector arrays, po-  
<sup>168</sup> sitioned around one of the collision points of the LHC. During the 2019-2022 Long Shutdown  
<sup>169</sup> of the LHC, the most complex upgrade of the ATLAS experiment is the replacement of the  
<sup>170</sup> small wheels of the muon spectrometer with the so-called New Small Wheels (NSWs) [5].

171 The detector upgrade addresses both the expected decrease in hit efficiency of the precision  
172 tracking detectors and the high fake trigger rate expected in the muon spectrometer at the  
173 HL-LHC. The NSWs are made of two different detector technologies: micromegas and small-  
174 strip thin gap chambers (sTGCs). Micromegas are optimized for precision tracking while  
175 sTGCs are optimized for rapid triggering, although each will provide complete coverage and  
176 measurement redundancy over the area of the NSWs. Eight layers each of sTGCs cover the  
177 NSWs. Practically, countries involved in detector constructor created quadruplet modules of  
178 four sTGCs glued together that were arranged and installed over the area of the NSWs once  
179 they arrived at CERN. Teams across three Canadian institutions built and characterized 1/4  
180 of all the required sTGCs.

181 The sTGCs are gas ionization chambers that consist of a thin volume of gas held between two  
182 cathode boards. One board is segmented into strip readout electrodes of 3.2 mm pitch. The  
183 position of the particle track in the precision coordinate can be reconstructed from the strip  
184 signals [5]. The sTGCs achieved the design track spatial resolution in the precision coordinate  
185 of less than 100  $\mu\text{m}$  per detector plane that will allow them to achieve a 1 mrad track angular  
186 resolution using the 8 layers of sTGC on the NSW [6, 5]. The NSW measurement of the  
187 muon track angle will be provided to the ATLAS trigger and used to reject tracks that do  
188 not originate from the interaction point [5].

189 The precise measurement of a muon track angle depends on knowing the position of each  
190 readout strip within the ATLAS coordinate system. To achieve this, the position of specific  
191 locations on the surface of sTGC quadruplets will be monitored by the ATLAS alignment  
192 system to account for time-dependent deformations [5]. Within a quadruplet module, the  
193 strip positions could have been shifted off of nominal by non-conformities of the strip pattern  
194 etched onto each cathode boards [7] and shifts between strip layers while gluing sTGCs into  
195 quadruplets.

196 An x-ray gun was used to measure the offset of strips from their nominal position at the  
197 locations that will be monitored by the ATLAS alignment system thereby providing, locally,  
198 an absolute “as-built” strip position within the ATLAS coordinate system. Estimates of the  
199 “as-built” positions of every readout strip are obtained by building an alignment model from  
200 the available x-ray measurements [8].

201 The technique of measuring the “as-built” strip positions using x-ray data has never been  
202 used before and must be validated. This thesis describes the use of cosmic muon data,  
203 recorded to characterize the performance of each Canadian-made sTGC module, to validate  
204 the x-ray strip position measurements. A description of how this work fits within the overall  
205 alignment scheme of the NSW is also presented.

206 Chapter 2 gives a brief overview of high energy particle physics necessary to understand the  
207 physics motivation of the HL-LHC and NSW upgrades. Chapters 3 and 4 present additional

208 details on the LHC, ATLAS, the NSWs, and sTGCs. In chapter [5](#), the cosmic ray testing  
209 procedure and how the position of the strips can be probed with cosmics data is presented.  
210 Chapter [6](#) introduces the x-ray method, and in chapter [7](#), the x-ray offsets are validated with  
211 cosmic muon data. The thesis concludes with a summary and outlook in chapter [8](#).

# <sup>212</sup> Chapter 2

## <sup>213</sup> High energy particle physics

<sup>214</sup> Particle physics aims to study the elementary constituents of matter. Understanding the fundamental building blocks and how they interact provides insight into how the early universe evolved to the forms of matter we observe today. This chapter introduces general concepts in particle physics relevant to understanding the physics goals of the High-Luminosity LHC (HL-LHC) and NSWs upgrade.

<sup>219</sup> The information on particle physics and the SM presented here is rather general; the interested reader is referred to [9, 10, 11] for more information.

### <sup>221</sup> 2.1 The Standard Model

<sup>222</sup> The Standard Model (SM) is a theoretical framework developed in the early 1970's that describes the observed elementary particles and their interactions. It is built on a collection of quantum field theories and has been remarkably successful at predicting experimental observations, including but not limited to the existence of the top quark [12], the tau neutrino [13] and the Higgs boson [14, 15].

<sup>227</sup> The known elementary particles described by the SM are represented in figure 2.1. There are 12 matter particles (six quarks and six leptons), 4 force-mediating particles, and the Higgs boson. Each matter particle also has an anti-matter particle pair with the same mass but opposite charge, not represented in figure 2.1. The different forces of nature are understood to be the result of the exchange of force-mediating particles between interacting (coupled) particles. Photons are mediators of the electromagnetic force, W<sup>+</sup>/- and Z bosons are mediators of the weak force, and gluons are mediators of the strong force. At high

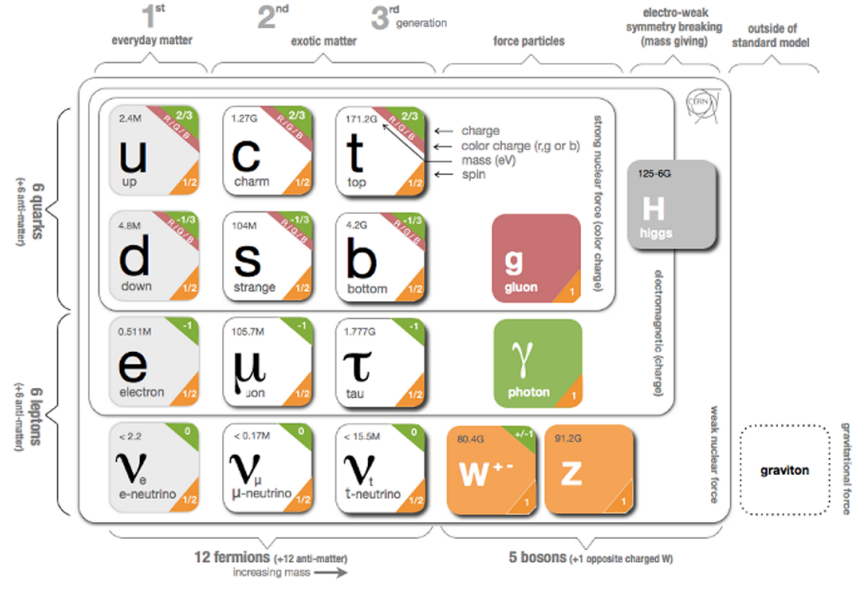


Figure 2.1: Schematic diagram of all elementary particles in the SM. Particles are grouped according to their properties and the forces through which they interact with other particles [16].

234 energy, the SM describes the electromagnetic and weak forces as stemming from a unified  
 235 electroweak force. The Higgs boson field interacts with the particles mediating the unified  
 236 electroweak force to distinguish the weak and electromagnetic forces from each other at lower  
 237 energies and give particles (except neutrinos) a mass. This is called electroweak symmetry  
 238 breaking.

239 Quarks are matter particles that are sensitive to all forces; notably they are the only particles  
 240 sensitive to the strong force. Protons and neutrons are made up of quarks and gluons, and the  
 241 strong force is responsible for their existence and mutual attraction into nuclei [17]. Leptons  
 242 are particles not sensitive to the strong force. Charged leptons include the electron, which  
 243 once part of atoms is responsible for chemistry. Of particular importance for this thesis is  
 244 the charged lepton called a muon. It is like the electron but its mass is  $\sim 200$  times larger  
 245 than that of the electron. Muons have a lifetime of  $2.2 \mu\text{s}$  [11] and decay predominantly as  
 246  $\mu \rightarrow e^- \bar{\nu}_e \nu_\mu$ . Neutrinos are neutral, almost massless leptons that only interact through the  
 247 weak force.

248 Common matter is made up of the lightest constituents of the SM: up and down quarks,  
249 electrons and photons. The other particles are produced in high-energy environments but  
250 then decay to the lightest constituents. Such high energy environments include the condi-  
251 tions present in the early universe [18], astrophysical sources, and particle accelerators. The  
252 presence of the particles of the SM at the beginning of the Universe means that their inter-  
253 actions and decays are fundamental for the study of the evolution of the early universe [18].  
254 Many high energy astrophysical sources, like supernovae, generate particles that rain down  
255 on Earth as cosmic rays [19]. Particle accelerators have been built to create controlled en-  
256 vironments of high-rate, high-energy particle collisions at high energy where the production  
257 and decay of elementary particles can be directly studied.

## 258 2.2 Beyond the Standard Model

259 Despite its success at describing most experimental observations to date, there is ample  
260 evidence that the SM is not a complete description of natural phenomena at the smallest  
261 scales. For example, the SM has a large number of free parameters, the values of which have  
262 to be fine-tuned to fit experimental observations. This is part of the so-called “naturalness”  
263 problem.

264 Furthermore, the SM provides no explanation for several open questions in particle physics.  
265 First, neutrinos in the SM are assumed to be massless and do not gain mass in the same way  
266 as the other particles. However, neutrino were confirmed to change between their different  
267 flavours in 2013 [20], which can only occur if neutrinos do have mass [21]. The neutrino  
268 mass requires physics beyond the standard model [22]. Second, several astrophysical and  
269 cosmological measurements suggest the presence of “dark matter” making up 85 % of the  
270 matter content of the universe [23]. The nature of dark matter is unknown and so far there  
271 is no SM explanation [24]. Third, the SM does not explain the origin and nature of the  
272 matter-antimatter asymmetry that produced our matter-dominated universe. Finally, the  
273 SM does not include a description of gravity.

274 Theoretical extensions beyond the Standard Model (BSM) aim to address some of these  
275 questions, often predicting existence of yet-unseen elementary particles or physics phenomena  
276 beyond those predicted by the SM. These hypothetical new physics phenomena or new  
277 particles can be searched for at particle accelerators.

278 **2.3 Studying high energy particle physics with accelerators**

- 280 In particular, particle accelerators of increasingly higher energy have a long history of enabling the discovery of predicted particles. These include, for example, the discovery of  
281 the W [25, 26] and Z bosons [27, 28], the top quark [29, 30], and most recently, the Higgs  
282 boson [31, 32]. The discovery of the Higgs boson marked the completion of the SM as it is  
283 known today.
- 284 Based on the established success of the SM, there are two approaches to particle physics  
285 research. One approach is to search for the existence of new physics phenomena predicted  
286 to exist in BSM theories and the other is to test the validity of the SM to a high degree of  
287 accuracy to search for flaws in the model. Standard Model predictions are generally expressed  
288 in terms of the probability of a specific physics process to occur, expressed as a cross section  
289 in units of barns (with 1 barn =  $10^{-28}$  m<sup>2</sup>). As an example, figure 2.1 shows a summary  
290 of cross section measured for different physics processes using the ATLAS experiment and  
291 their comparison with the predictions of the SM. Most cross section measurements agree  
292 well within one standard deviation with the SM predictions.
- 293 Particle accelerators provide a controlled and high-collision rate environment that makes  
294 them ideal places to search for new physics phenomena and to carry out systematic tests of  
295 the SM. The LHC is the highest energy collider in the world so it can access physics that  
296 no other accelerator can. A description of the LHC and the ATLAS detector are provided  
297 in the next chapter.

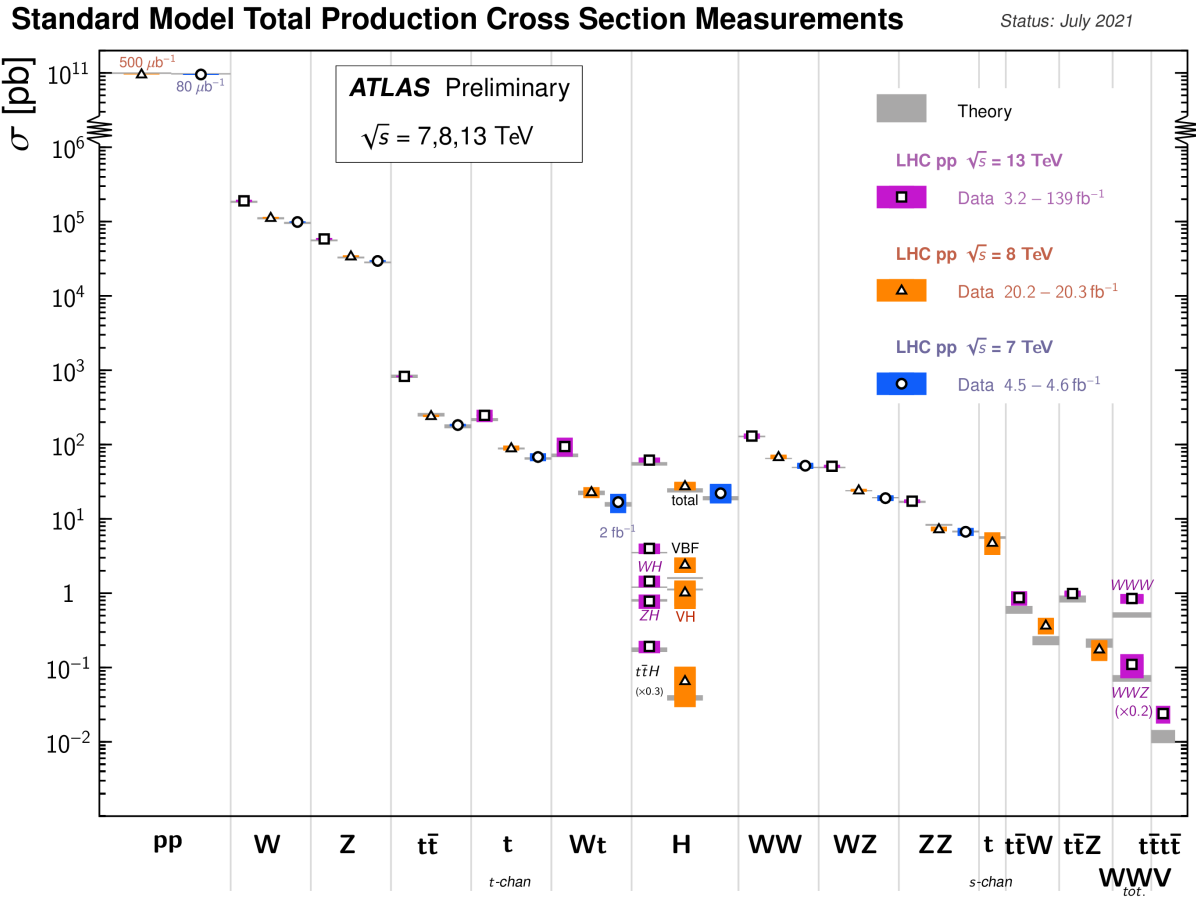


Figure 2.2: Production cross sections of different final states measured by the ATLAS experiment at the LHC. Comparison with the SM theory predictions is also shown [33].

299 **Chapter 3**

300 **The LHC and the ATLAS experiment**

301 The Large Hadron Collider (LHC) is the world’s most energetic particle accelerator and the  
302 ATLAS experiment is used to record the results of particle collisions at the LHC. In this  
303 chapter, details about both that are necessary to understand the High-Luminosity LHC (HL-  
304 LHC) upgrade project and the ATLAS experiment’s New Small Wheels (NSWs) upgrade  
305 are presented.

306 **3.1 The Large Hadron Collider**

307 The LHC is an accelerator 27 km in circumference and located  $\sim$ 100 m underground at  
308 the CERN laboratory near Geneva, Switzerland [1]. It has two beam pipes within which  
309 bunches of protons counter-circulate before being collided in the center of one of four major  
310 experiments, such as the ATLAS experiment (discussed in section 3.3). Protons are guided on  
311 the circular trajectory using 1232 superconducting dipole magnets capable of a maximum  
312 field of 8.33 T. Radio-frequency accelerating cavities are used to accelerate protons to a  
313 the maximum design energy of 7 TeV [34]. During LHC Run-1 (2011-2012), protons were  
314 collided at a collision center-of-mass energy of 7 TeV and 8 TeV [35]. During LHC Run-2  
315 (2015-2018), the center-of-mass energy of proton collisions was increased to 13 TeV [36],  
316 close to the maximum design value of 14 TeV [34]. It is not actually the protons that  
317 interact, but the constituent quarks and gluons that each carry some fraction of the energy  
318 and momentum of the collisions.

319 **Luminosity**

320 The number of proton-proton interactions generated by the LHC directly affects the statistics

available to make measurements of interaction cross sections. Predicting the number of proton-proton interactions requires defining a metric called luminosity [11]. The luminosity of a particle collider is the number of particles an accelerator can send through a given area per unit time. It is calculated from the measurable quantities in Equation 3.1:

$$\mathcal{L} = \frac{f N_1 N_2}{4\pi\sigma_x\sigma_y}, \quad (3.1)$$

where  $f$  is the frequency of the bunch crossings (25 ns),  $N_1$  and  $N_2$  are the number of protons in each bunch ( $\sim 10^{11}$  protons / bunch), and  $\sigma_x$  and  $\sigma_y$  are the RMS of the spatial distributions of the bunch. Therefore, luminosity is a property of accelerator beams, which are set by the capabilities of the accelerator. The design luminosity of the LHC was  $10^{34} \text{ cm}^{-2}\text{s}^{-1}$ . The units of luminosity are an inverse area; multiplying the luminosity by the cross section of a given process gives the expected rate for that process.

Integrating the *instantaneous* luminosity (equation 3.1) over a period of data collection time gives the integrated luminosity,

$$L = \int \mathcal{L}(t) dt \quad (3.2)$$

which is related to the total number of interactions. In this way, the luminosity is the link between the accelerator and the statistical power of measurements to be made with the data collected. So far, the LHC provided an integrated luminosity of  $28.26 \text{ fb}^{-1}$  in Run-1 [35] and  $156 \text{ fb}^{-1}$  in Run-2 [36].

## 3.2 The High-Luminosity LHC

At the end of the LHC program in 2025, the statistical gain on measurements in running the LHC further will become marginal. The HL-LHC [2] project consists of the upgrade of LHC infrastructure to achieve a nearly ten fold increase in instantaneous luminosity, thereby improving measurement statistics as well. Also, some systems will need repair and replacement to operate past  $\sim 2020$ . The LHC will continue to be the most energetic accelerator in the world for years to come and is the only accelerator with enough energy to directly produce the Higgs boson and top quarks. Therefore, the European Strategy for Particle Physics made it a priority “to fully exploit the physics potential of the LHC” with “a major luminosity upgrade” [37]. The goal is for the HL-LHC to provide an integrated luminosity of  $3000 \text{ fb}^{-1}$  in the 12 years following the upgrade. The luminosity actually



Figure 3.1: The LHC/HL-LHC timeline [38]. The integrated luminosities collected and projected for each run of the LHC are shown in blue boxes below the timeline and the center of mass energy of the collisions is shown in red above the timeline. The top blue arrow labels the run number. The acronym “LS” stands for “long shutdown” and indicates periods where the accelerator is not operating. During the shutdowns, upgrades to the LHC and the experiments are taking place. This timeline was last updated in January, 2021, and reflects changes in the schedule due to the ongoing pandemic.

348 achieved will depend on a combination of technological advances and upgrades in progress  
 349 that affect the factors contributing to luminosity defined in equation 3.1 [2]. Figure 3.1 shows  
 350 the projected schedule of the HL-LHC upgrades and operation [38].

351 One of the most anticipated measurements at the HL-LHC is the value of the triple-Higgs  
 352 coupling. Measuring the coupling will allow the determination of the shape of the Higgs  
 353 potential responsible for electroweak symmetry breaking. Any discrepancy with respect to  
 354 the SM prediction will show that there must be other sources of electroweak symmetry  
 355 breaking, and hence physics phenomena beyond the SM. The LHC is the only accelerator  
 356 where the Higgs boson can be produced directly so it is the only place where the triple-Higgs  
 357 coupling could be measured. The HL-LHC upgrade is required to produce a significant  
 358 sample of Higgs produced in pairs to make a statistically meaningful measurement [3, 39].

359 Accordingly, detector sensitivity to various Higgs decays will be important at the HL-LHC.

### 360 3.3 The ATLAS experiment

361 The ATLAS experiment [4] was designed to support all the physics goals of the LHC. It  
362 is 44 m long and 25 m in diameter, and weighs 7000 tonnes. The ATLAS experiment is  
363 centered around one of the LHC's interaction points (a place where the beams collide). As  
364 shown schematically in figure 3.2, ATLAS consists of an array of particle detector subsystems  
365 arranged concentrically around the beam pipe. The ATLAS experiment is cylindrical because  
366 it aims to provide  $4\pi$  coverage around the interaction point. In reference to the cylindrical  
367 geometry of the experiment, it is helpful to separate the subsystems of ATLAS into the  
368 so-called "barrel" and "endcap"/"forward" regions.

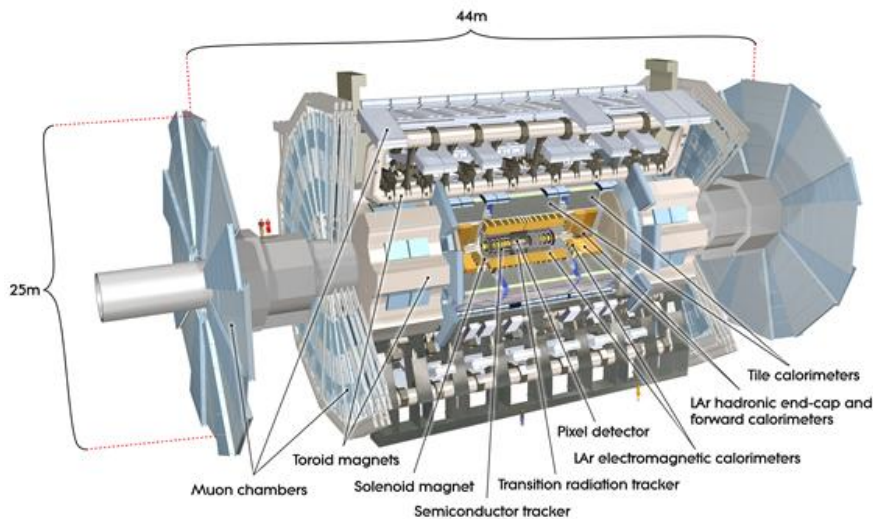


Figure 3.2: Schematic diagram of the ATLAS experiment, with the various detector subsystems labelled [4].

369 For analysis purposes, a spherical coordinate system is defined. The azimuthal angle  $\phi$  is  
370 measured around the beampipe and the polar angle  $\theta$  is measured from the beam pipe. The  
371 polar angle is more often expressed in terms of pseudo-rapidity, defined as  $\eta = -\ln \tan(\theta/2)$ .  
372 Pseudo-rapidity values vary from 0 (perpendicular to the beam) to  $\pm\infty$  (parallel to the  
373 beam, defined as the z-direction) and is an approximation to the rapidity of a particle when  
374 its momentum is much greater than its mass. It is useful to describe the direction of outgoing

375 particles in proton-proton collisions because differences in rapidity are invariant to a Lorentz  
376 boost along the beam direction.

377 The ATLAS experiment provides identification and kinematic measurements for each particle  
378 created after the initial collision, which is done by assembling offline the information recorded  
379 by each subsystem. With this information, signatures of processes of interest can be identified  
380 and studied. An overview of the main ATLAS subsystems is given below.

### 381 **The inner detector**

382 The inner detector [40, 41] (figure 3.3) is for precise measurements of charged particle tra-  
383 jectories, measurement of primary and secondary interaction vertices and assistance in the  
384 identification of electrons. A 2 T solenoid with field parallel to the beam bends the trajec-  
385 tory of outgoing charged particles. A measurement of the bending radius of each charged  
386 particle provides information about its momentum. The innermost part of the inner tracker  
387 is made of high-resolution semiconductor pixel and strip detectors while the outermost part  
388 is made of straw-tubes. The straw tubes are used in the trajectory measurements but they  
389 are also interspersed with material designed to enhance the creation of transition radiation.  
390 Transition radiation occurs when a highly relativistic charged particle traverses a material  
391 boundary [42]. The amount of transition radiation emitted by a charged particle is detected  
392 by the straw-tubes and is used to identify electrons.

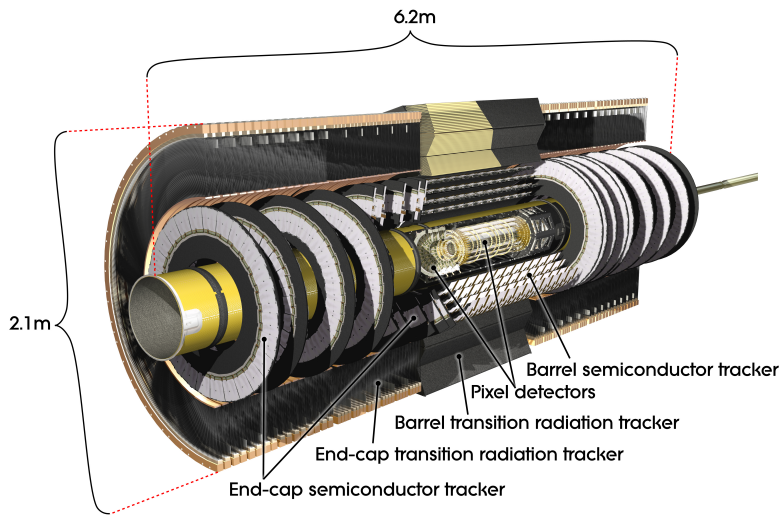


Figure 3.3: Schematic diagram of the ATLAS experiment's inner detector, with the different segments and the technology used labeled [4].

393 **Calorimetry system**

394 Electromagnetic and hadronic sampling calorimeter units are used to record the energy  
395 of electrons, photons and jets<sup>1</sup>. A combination of liquid-argon (LAr) electromagnetic and  
396 hadronic calorimeters [43] and tile-scintillator hadronic calorimeters [44] cover the rapidity  
397 range  $|\eta| < 4.9$ , as shown in figure 3.4.

398 Sampling calorimeters have alternating layers of dense material and material that can mea-  
399 sure the amount of ionization by charged particles. The dense material causes incoming  
400 charged particles to shower into lower energy particles and deposit their energy in the sen-  
401 sitive volume. Only muons and neutrinos are known to pass the calorimeters to the muon  
402 spectrometer without being absorbed.

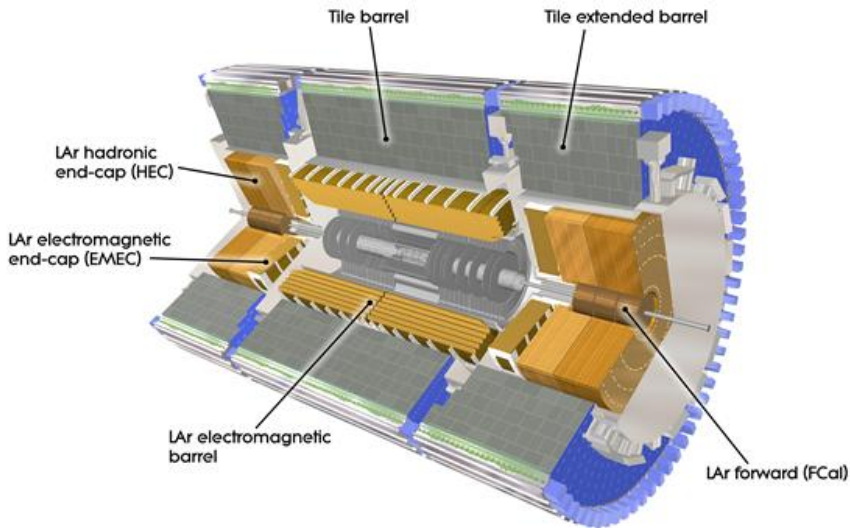


Figure 3.4: Schematic diagram of the ATLAS calorimeter system, with the different segments and the technology used labeled [4].

403 **Muon spectrometer**

404 The muon spectrometer [45] consists of multiple layers of tracking chambers embedded in  
405 a 2 T magnetic field generated by an air-core superconducting toroid magnet system. Fig-  
406 ure 3.5a shows a schematic diagram of the layout of the different chambers and of the toroid

<sup>1</sup>When quarks or gluons are expelled in a high energy collision, they create collimated groups of hadrons called jets because they carry a charge called “colour”, and nature only allows “colourless” combinations to exist [42].

407 magnets [4]. The trajectory of a muon is reconstructed from the information recorded by  
 408 the different types and layers of tracking chambers. The amount of bending in the magnetic  
 409 field provides a measure of the muon's momentum. In the barrel section of ATLAS, the  
 410 toroidal magnetic field is created by eight coils bent into the shape of a "race-track" and  
 411 symmetrically arranged around the beampipe. In the forward region, two end-cap toroids,  
 412 each with eight smaller racetrack-shaped coils arranged symmetrically around the beam pipe  
 413 are inserted in the ends of the barrel toroid [46].

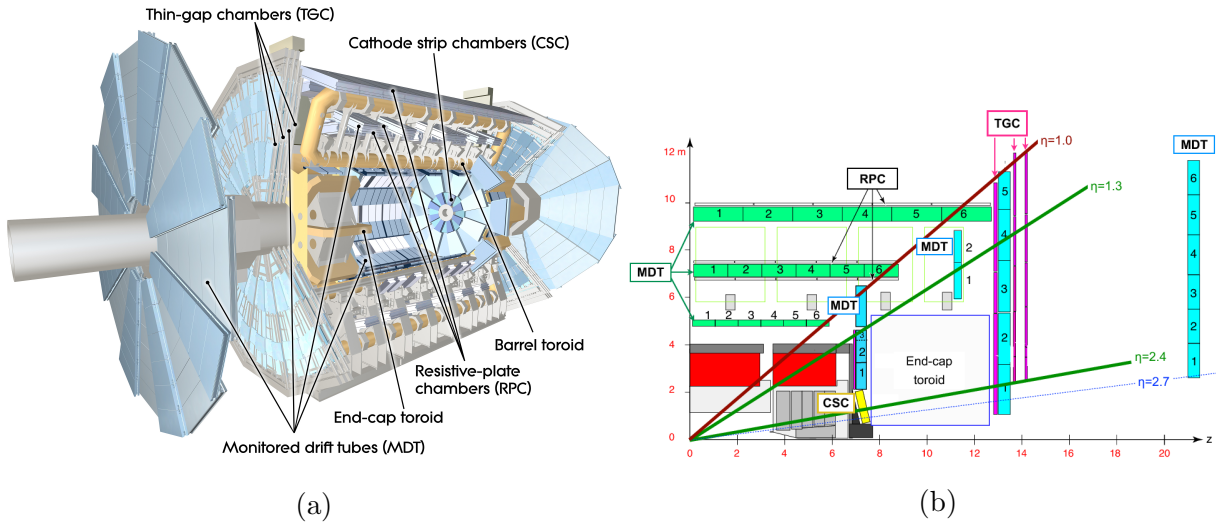


Figure 3.5: Schematic diagram of the ATLAS muon spectrometer. Figure (a) shows a 3D projection of the system with the different types of chambers and different parts of the toroidal magnet system labeled [4]. Figure (b) shows a projection of one quarter of the muon spectrometer, with the interaction point in the bottom left corner. The small wheel is just left of the end cap toroid, the big wheel is to its right, and the outer wheel is the rightmost structure [47].

414 The muon spectrometer is separated into detectors used for precision offline tracking and  
 415 for triggering purposes. Three layers of monitored drift tubes (MDTs) or cathode strip  
 416 chambers (CSCs) are used for tracking. The position of the muon track in each of the three  
 417 layers allows reconstruction of the bent trajectory of a muon and hence its momentum. To  
 418 satisfy the muon spectrometer target momentum resolution of  $\Delta p_T/p_T < 1 \times 10^{-4} p / \text{GeV}$   
 419 for  $p_T < 300 \text{ GeV}$  and a few percent for lower  $p_T$  muons, the MDTs and CSCs were designed  
 420 to achieve a spatial resolution of  $50 \mu\text{m}$  each. Accordingly, an optical alignment system was  
 421 designed to monitor and correct for chamber positions [45, 48].

422 Resistive plate chambers (RPCs) are used for triggering in the barrel and thin-gap chambers

423 (TGCs) are used for triggering in the endcaps. The positions of each type of chamber  
424 are sketched in figure 3.5b. The endcap section of the muon spectrometer consists of three  
425 sections, the small wheel, big wheel, and outer wheel – ordered by proximity to the interaction  
426 point. In Run-1, low (high)  $p_T$  muons were triggered on if two (three) of the RPC or TGC  
427 layers around the big wheel fired in coincidence, for the barrel and endcaps respectively [49].  
428 After Run-1 it was discovered that up to 90% of the triggers in the endcap were fake, caused  
429 by background particles generated in the material between the small wheel and the big  
430 wheel [5]. To reduce the fake rate in Run-2, the TGCs on the inside of the small wheel also  
431 had to register a hit. The added condition reduced the trigger rate by 50% in the range  $1.3 < |\eta| < 1.9$  [50]. The effectiveness of the solution was limited since the  $|\eta|$ -range of the small  
433 wheel TGCs was limited to  $1.0 < |\eta| < 1.9$  and the spatial resolution of the small wheel  
434 TGCs is coarse [5].

### 435 Trigger system

436 It would be impossible to record all the data from bunch crossings every 25 ns, corresponding  
437 to a rate of  $\sim 40$  MHz. The ATLAS experiment has a multi-level trigger system to select  
438 events of interest for permanent storage. The Level-1 (L1) hardware trigger [49] uses partial-  
439 granularity information from the muon spectrometer and calorimeters to trigger on high  $p_T$   
440 muons, electrons, jets, missing transverse energy, and  $\tau$  decaying to hadrons. After Run-3  
441 an upgrade of the trigger system will allow a maximum trigger rate of 1 MHz with a latency  
442 of 10  $\mu$ s [51], but for now the working limits are a rate of 100 kHz [50] and 2.5  $\mu$ s [49].

443 The L1 trigger is used to define regions of interest that are fed into the software high level  
444 trigger (HLT) [52], in which the full granularity of the muon spectrometer and calorimeter  
445 are used with information from the inner detector to reduce the trigger rate to 1 kHz. Events  
446 that satisfy at least one of the L1 and HLT trigger criteria are recorded to permanent storage  
447 for offline analysis.

448

---

449 With the foreseen increase in luminosity at HL-LHC, it is a priority to upgrade the ATLAS  
450 detector to further reduce the muon trigger fake rate in the forward region. The New Small  
451 Wheels being commissioned to replace the original ATLAS muon small wheels will address  
452 this challenge.

453 **Chapter 4**

454 **The New Small Wheels**

455 **4.1 Motivation for the New Small Wheels**

456 The hit rate of all detector systems will significantly increase during HL-LHC operation  
457 because of the increase in luminosity. The increased rate presents a challenge for both the  
458 tracking and triggering capabilities of the muon spectrometer [5].

459 In terms of precision tracking, the maximum hit rate in the MDTs is expected to reach above  
460 300 kHz by the end LHC operation. At this rate, the hit efficiency of MDTs decreases by  
461 35%, mostly due to the long dead-time of the chambers. Losing hits in the small wheel will  
462 reduce the high  $p_T$  muon momentum resolution. The decrease in resolution will affect the  
463 ability to search for, for example, the decay of hypothetical heavy bosons ( $W'$ ,  $Z'$ ) or other  
464 hypothetical particles beyond the SM [3].

465 Already during LHC Run-2 operation, the forward muon trigger system had to cope with a  
466 very high fake rate, even with the inclusion of TGC data from the small wheel as part of the  
467 trigger criteria. At the luminosity expected in Run-3, it is estimated that 60 kHz out of the  
468 maximum L1 trigger bandwidth of 100 kHz would be taken up by forward muon triggers.  
469 To address this challenge, a possible solution would be to raise the minimum  $p_T$  threshold  
470 from 20 GeV to 40 GeV. However, this would have an adverse impact on the ability to study  
471 several physics processes of interest that depend on low  $p_T$  muons, particularly the Higgs  
472 decay to two muons, the Higgs decay to two tau leptons and hypothetical particle decays  
473 beyond the SM [5].

474 The NSWs will address both of these problems. They will be made of precision tracking  
475 chambers suitable for the expected hit rates during the HL-LHC and triggering chambers  
476 capable of 1 mrad track angular resolution. The idea behind the design triggering capability



Figure 4.1: A schematic diagram of a quarter cross section of the ATLAS muon spectrometer, with the interaction point (IP) in the bottom left corner. Three possible tracks are labeled. Ideally, track A would be triggered on while track B and C discarded. With the old small wheel, all three tracks would be recorded. With the NSW, only track A would be recorded [5].

477 of the chambers is to allow matching of track segments measured by the NSW with track  
 478 segments from the big wheel to discard tracks not originating from the interaction point.  
 479 Figure 4.1 illustrates this point: the Run-2 trigger system would have triggered on all three  
 480 tracks (A, B, C) while with the NSW the trigger system would only trigger on track A.  
 481 The NSWs will therefore make it possible to maintain a low muon  $p_T$  trigger threshold and  
 482 maintain an adequate muon momentum resolution during HL-LHC operations, which will  
 483 allow the full exploitation of the physics potential of this research program [5].



(a) A sTGC quadruplet module. The left image highlights the trapezoidal shape of a quadruplet module. The right image shows the corner at the short edge, where the four sTGC layers and each layer's gas inlet are visible. The gas outlets and high voltage cables are located along the long edge near the corner in the back left of the photo. The green printed circuit board along the sides are the adaptor boards where the front end electronics are attached.



(b) Left: A sTGC wedge. The white frame outlines the individual quadruplet modules that have been glued together into a wedge. Right: A completed sector, with two sTGC wedges on the outside and two micromegas wedges on the inside.



(c) A picture of one of the two NSWs. All sectors except one large sector at the top are installed, revealing two of the smaller sectors that are normally hidden under the large sectors and support bars. The NSWs are 9.3 m in diameter.

Figure 4.2: Images showing different stages of NSW construction.

484 **4.2 Design of the NSWs**

485 The NSWs are made with two detector technologies: micromegas and small-strip thin gap  
486 chambers. Eight layers of each cover the entire area of the wheel. Micromegas are designed  
487 to be the primary precision tracking detectors and sTGCs the primary triggering detectors,  
488 but both technologies offer full redundancy by being capable of providing both precision  
489 measurements and trigger information. Both types of detectors were designed to achieve  
490 spatial resolution better than  $\sim 100 \mu\text{m}$  per layer. Four chambers are glued together to create  
491 quadruplet modules of each detector type. Quadruplets of different sizes, most shaped as  
492 trapezoids, are assembled into wedges. Two sTGC wedges and two micromegas wedges are  
493 layered to create sectors (with the sTGC wedges on the outside) [5]. Different stages of the  
494 construction process are shown in figure 4.2. At the time of writing, the assembly of the  
495 NSWs has just been completed. The first NSW has been lowered into the ATLAS cavern  
496 and is being commissioned and the second will be lowered shortly.

497 **4.3 Small-strip thin gap chambers**

498 The sTGCs are gas ionization chambers operated with a gas mixture of CO<sub>2</sub>:n-pentane with  
499 a ratio of 55%:45% by volume. Gold-plated tungsten wires, 50  $\mu\text{m}$  in diameter and with  
500 1.8 mm pitch, are suspended between two cathode planes made of FR-4, each 1.4 mm away  
501 (see figure 4.3). One cathode board is segmented into copper pads of varying area (with a  
502 typical size of  $\sim 300 \text{ cm}^2$  each), and the other is segmented into copper strips of 3.2 mm pitch  
503 running lengthwise perpendicular to the wires. High voltage is applied to the wires and the  
504 cathode planes are grounded [5, 53]. When a muon passes through a sTGC, it will ionize some  
505 of the atoms in the gas and the electric field in the gas gap will result in the formation of an  
506 ionization avalanche [54]. The motion of the ions and free electrons generates small currents  
507 on the nearby wire and capacitatively-coupled strip and pad electrodes [5]. The gas mixture  
508 was chosen to absorb excess photons produced in the avalanche that delocalize the avalanche  
509 signal [55] and saturate many strip electrodes, preventing the formation of streamers [42].  
510 This allows the chambers to be run at a higher high-voltage providing a faster response and  
511 higher signal [55]. The resistivity of the carbon coating and capacitance of the pre-preg  
512 sheet tune the spread of the charge distribution [56] and the speed of the response [57] to  
513 optimize the rate capability. The combined information from the strip readout electrodes  
514 and wires provide the location where the muon passed through the chamber. The small pitch  
515 of the strip readout electrodes is what allows the quadruplets to deliver good track angular  
516 resolution to improve the fake trigger rate and meet the precision tracking requirements [5].



Figure 4.3: Internal structure of an sTGC, zoomed into the area under a pad. High voltage is applied to wires suspended in the gas volume to create an electric field. A passing muon causes an ionization avalanche that is picked up by the wire, strip and pad electrodes [8].

- 517 A 3-out-of-4 coincidence in pad electrodes from each layer of a quadruplet defines a region of  
 518 interest where the strip and wire electrodes should be read out. The pad triggering scheme  
 519 greatly reduces the number of electrodes that require readout so that a track segment of the  
 520 required angular resolution can be provided quickly enough to the hardware trigger [5].
- 521 Signal is read out from groups of successive wires, so the position resolution in the direction  
 522 perpendicular to the wires is 10 mm per plane. The wires give the azimuthal coordinate  
 523 in ATLAS so the position resolution in this direction is sufficient. Good resolution on the  
 524  $\eta$  coordinate, perpendicular to the strips, is important [5]. In a test beam environment,  
 525 the strip spatial resolution of a single sTGC was measured to be 45 microns for muon  
 526 perpendicularly incident on the surface of the sTGC. Although the spatial resolution worsens  
 527 as function of muon angle measured from normal incidence [58], when four sTGCs are glued  
 528 together into a quadruplet the design angular resolution of 1 mrad in the strip coordinate is



(a) Brass insert near long edge.

(b) Brass insert near short edge.

Figure 4.4: The brass inserts sticking out from the gas volumes of an sTGC quadruplet. These inserts were pressed against alignment pins when the individual sTGCs were being glued together.

529 achievable [5, 53].

530 To achieve the required track angular resolution once installed in ATLAS, the absolute  
 531 position of each sTGC strip within the ATLAS coordinate system must be accurately known.  
 532 The degree of accuracy required is on the order of the position resolution of the chambers,  
 533  $\sim 100 \mu\text{m}$ . The NSW alignment system, detailed in section 4.5, will monitor the position of  
 534 alignment platforms installed on the surface of the wedges. The alignment platforms are  
 535 installed with respect to an external reference on the sTGCs: two brass inserts on each strip  
 536 layer on one of the angled sides of each quadruplet (shown in figure 4.4). So the challenge  
 537 of monitoring the position of the strips in ATLAS was separated into two steps: first, infer  
 538 the position of the strips with respect to the brass inserts using the sTGC design geometry;  
 539 second, use the alignment system to monitor the position of the alignment platforms. The  
 540 next section provides some pertinent details on the sTGC construction process, with steps  
 541 that affect the position of the strips with respect to the brass inserts highlighted.

## 542 4.4 sTGC Quadruplet Construction

543 Five countries were responsible for producing sTGC quadruplets of varying geometries for the  
544 NSW: Canada, Chile, China, Israel and Russia. Canada was responsible for the construction  
545 of one quarter of the required sTGCs, of three different quadruplet geometries. The steps of  
546 the construction process in each country were similar [5]. The process followed in Canada is  
547 detailed here.

548 A research group at TRIUMF in Vancouver, British Columbia was responsible for preparing  
549 the cathode boards. The boards were made and the electrodes etched on at a commercial  
550 laboratory, Triangle Labs, in Carson City, Nevada. Once completed they were sent to TRI-  
551 UMF to be sprayed with graphite and to have support structures glued on [7]. The boards  
552 are commercial multilayer printed circuit boards, but the strip boards required precision ma-  
553 chining to etch the strip pattern [5]. Triangle Labs also machined the two brass inserts into  
554 each strip board. A coordinate measuring machine (CMM) was used to accurately measure  
555 the position of a set of reference strips on each board. Four quality parameters describing  
556 non-conformities in the strip pattern of each board with respect to the brass inserts were  
557 derived from the data and the results are available on a QA/QC database. The parameters –  
558 offset, angle, scale and nonparallelism – and the CMM data collection is described in full  
559 in [7]. Due to time constraints, tolerances on the non-conformities in the etched strip pattern  
560 with respect to the brass inserts were loosened, with the condition that the strip positions  
561 in ATLAS would have to be corrected for [7].

562 The prepared boards were sent to Carleton University in Ottawa, Ontario for construction  
563 into sTGCs and quadruplets. First, the wires were wound around the pad cathode boards  
564 using a rotating table and the wires were soldered into place. A wound pad cathode board glued  
565 was held by vacuum on a granite table, flat to within 20  $\mu\text{m}$ , and a strip cathode board glued  
566 on top to create an sTGC. Holding one sTGC flat with the vacuum, another was glued on  
567 top to create a doublet, then two doublets were glued together to create a quadruplet. When  
568 gluing sTGCs together, the brass inserts were pushed against alignment pins with the goal of  
569 keeping the strip layers aligned within tolerance. However, non-conformities in the shape of  
570 the brass inserts, non-conformities in the position of the alignment pins and shifts between  
571 sTGCs while the glue cured resulted in misalignments between the brass inserts and strip  
572 layers. Precise alignment of the pad boards or wires with respect to the strip boards did  
573 not have to be so tightly controlled because pads and wires do not measure the precision  
574 coordinate.

575 The Carleton team finished the quadruplets by installing adaptor boards on the angled sides  
576 of each layer that allow front end electronics to be attached. Completed quadruplets were  
577 sent to McGill University where their performance was characterized with cosmic rays. De-

578 tails pertaining to cosmic ray testing of sTGC quadruplets at McGill University are described  
579 in chapter 5. Tested quadruplets were sent to CERN where they were assembled into wedges  
580 and alignment platforms installed. The alignment platforms were installed using a jig posi-  
581 tioned with respect to the brass inserts. Completed wedges were assembled into sectors then  
582 installed on the NSWs.

583 The quadruplet construction process had two steps where strip positions could be shifted off  
584 of nominal. At board-level, there could be non-conformities in the etched strip pattern with  
585 respect to the brass inserts, described by the four quality parameters [7]. At the quadruplet  
586 level, misalignments between the brass inserts and strips on different layers were possibly  
587 introduced during the gluing. The result was that the brass inserts were not a reliable  
588 reference point and that the strips can be offset from their design position by up to hundreds  
589 of micrometers. Offsets in strip positions from nominal in Canadian quadruplets were shown  
590 to be random [7], so no one correction would suffice. The offsets must be measured and  
591 corrected for in the ATLAS offline software that does the precision tracking. Understanding  
592 the work ongoing to make measurements of strip position offsets and correct for them requires  
593 understanding the strategy of the NSW alignment system.

## 594 4.5 NSW alignment

595 The idea of the NSW alignment system is presented in [5], but the details have only been  
596 presented internally so far. After the wedges are constructed, alignment platforms are in-  
597 stalled on every sTGC quadruplet and optical fibres routed to them, as shown in figure 4.5.  
598 Light from the optical fibres will be monitored in real time by cameras (BCAMs) mounted on  
599 the alignment bars of the NSWs. The system will thus record the positions of the alignment  
600 platforms in the ATLAS coordinate system and any changes over time.

601 The original alignment scheme was to use the brass inserts as a reference between the align-  
602 ment platforms and the individual strips, as shown in the solid arrows in figure 4.6 – this  
603 will no longer work. The position of the alignment platforms will be known thanks to the  
604 alignment system, so a different method to get the position of the strips with respect to the  
605 alignment platforms is currently in its final stage of development. The technique consists of  
606 the measurement of the strip pattern offset at a few areas on the surface of a sTGC quadru-  
607 plet using an xray gun mounted on the alignment platforms. The local strip pattern offset  
608 with respect to nominal geometry at the location of each alignment platform is obtained  
609 by analyzing the xray gun beam profile. As shown in figure 4.6, this approach essentially  
610 bypasses the need to know the position of strips with respect to the brass inserts. The align-  
611 ment platforms provide the link to the nominal geometry because the nominal group of strips

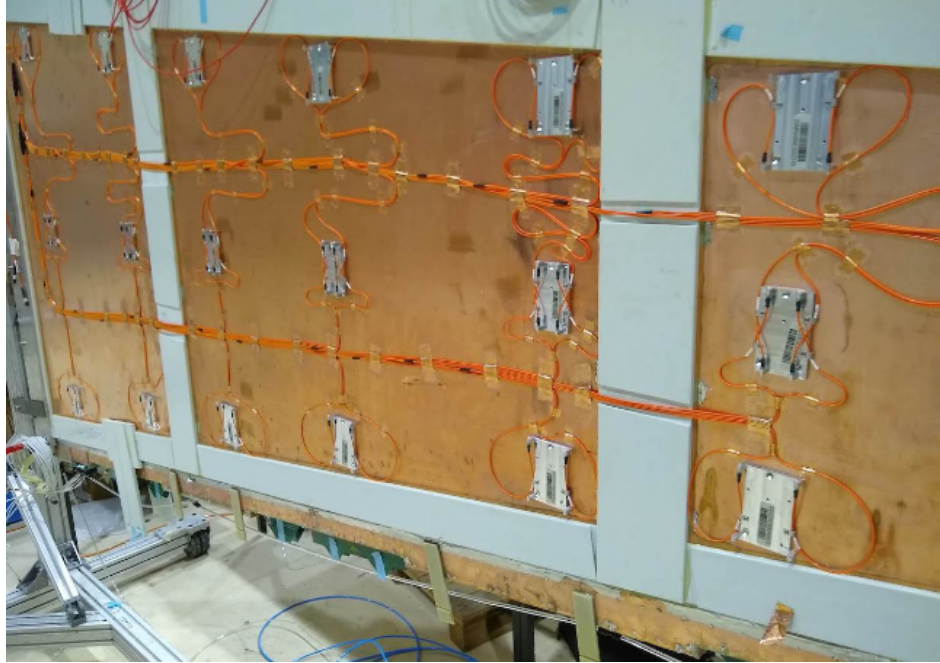


Figure 4.5: A sTGC wedge with alignment platforms (silver) installed on the quadruplet. Optical fibres (orange) are routed to the alignment platforms. Cameras on the frames of the NSWs will record light from the optical fibres to monitor in real-time the position the alignment platforms in the ATLAS coordinate system.

612 that should be nearest to them can be identified using the nominal geometry parameters that  
 613 assume the strips are perfectly etched and aligned. Cosmic muon track positions cannot be  
 614 compared to the nominal geometry because the alignment platforms are not installed when  
 615 cosmics data is collected, so there is no external reference to provide a link to the nominal  
 616 geometry.

617 The x-ray method does not have the sensitivity to measure the offset of each strip from  
 618 nominal, but what can be measured instead is the offset of the strip pattern in a local area  
 619 around the position of the gun. *Local offsets* are used to build an alignment model for each  
 620 strip layer. Formally defined, an alignment model is a set of parameters used to estimate the  
 621 “as-built” position of a strip given its nominal position. The alignment model currently being  
 622 worked on takes x-ray and CMM data as input to calculate an overall offset and rotation of  
 623 each strip layer with respect to nominal [8]. The alignment parameters could be described  
 624 as “global”, meaning over the whole layer instead of local. Without the x-ray dataset, there  
 625 would be no input to the alignment model that takes into account inter-layer misalignments  
 626 introduced during quadruplet construction.

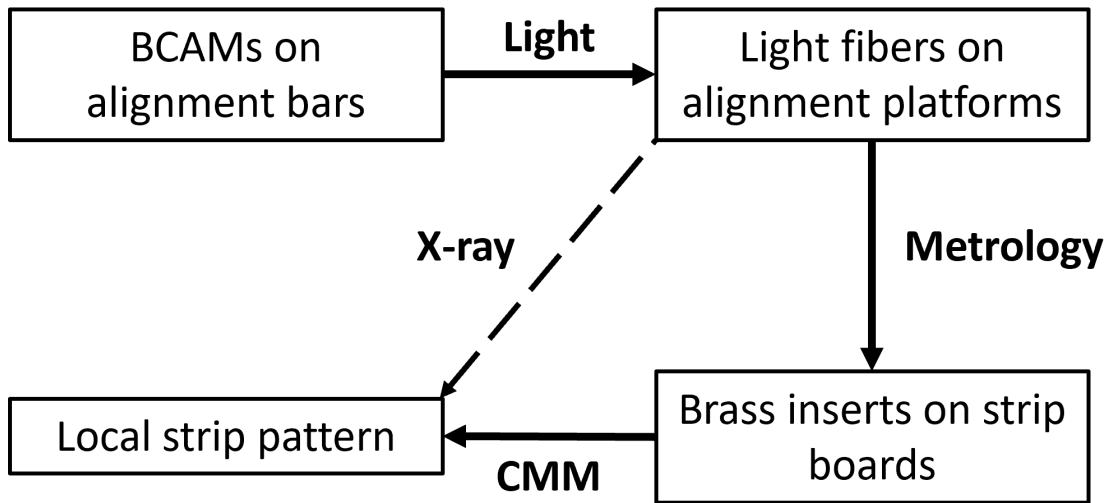


Figure 4.6: Schematic diagram showing how the different elements of the sTGC alignment system relate to one another. The solid arrows denote the planned alignment scheme. The dashed arrow shows the modification being finalized now. This figure was originally designed by Dr. Benoit Lefebvre.

Given that the x-ray local offsets can only be measured at positions where the gun can be attached and that they are an important part of the alignment scheme, the new x-ray measurement technique needs to be validated. The goal of this thesis is to validate the x-ray local offsets while exploring how cosmics data complements and adds to the understanding of strip positions and global alignment.

# 632 Chapter 5

## 633 Using cosmic muons to measure 634 relative strip position offsets

635 At McGill University, among other quality and functionality tests, each Canadian-made  
636 quadruplet was characterized with cosmic muons. In this chapter, the experimental setup and  
637 how the data was analyzed to provide relative strip position offsets is presented. The analysis  
638 method was motivated by the how the measurements could be compared to measurements  
639 done with the x-ray method (chapter 6) but also it stands alone as a characterization of the  
640 alignment between strips of different layers. The chapter begins with a brief introduction to  
641 cosmic rays.

### 642 5.1 Cosmic rays

643 The earth is being constantly bombarded by particles from the sun, galactic sources and  
644 extra galactic sources – collectively called cosmic rays [19, 11]. Cosmic rays consist mostly  
645 of protons, but also heavier ions, gamma rays and the term sometimes includes neutrinos.  
646 The primary (initial) cosmic ray interacting with the atmosphere causes electromagnetic and  
647 hadronic showers of secondary particles. Hadronic showers result from the primary cosmic ray  
648 interacting strongly with the target of the atmosphere, resulting in an abundant production  
649 of pions. Charged pions predominantly decay to muons (there is a lesser contribution to  
650 the muon flux from kaons as well) [59]. The secondary muons are relativistic and thanks  
651 to time dilation their lifetime is extended as measured in the reference frame of earth, so a  
652 flux of approximately 1 muon/cm<sup>2</sup>/ min reaches the ground [11]. Measuring the muon flux  
653 and energy spectrum reveals information about primary cosmic rays [59] which is interesting

654 to high energy physicists and astrophysicists. The muon flux is also terribly convenient for  
655 testing muon detectors.

656 **5.2 Experimental setup**



Figure 5.1: Cosmic muon hodoscope at McGill University with a sTGC quadruplet module in the test bench.

657 Cosmic muon characterization of sTGC quadruplet modules was done with a hodoscope, a  
658 complete description of which can be found in [58]. The quadruplet was placed in the center  
659 of the test bench. Above and below it was a layer of scintillator-PMT arrays, as shown in  
660 figure 5.1. When a cosmic muon passed within the acceptance of the hodoscope, at least one  
661 scintillator from the top array and at least one from the bottom array fired in coincidence.  
662 A trigger signal was formed using NIM modules from the coincidence of signals from the top

663 and bottom arrays of scintillators. The trigger signal was passed to the front-end electronics  
664 attached to the adaptor boards of each layer of the quadruplet.

665 Operating the chambers also required gas and high voltage. A gas mixture of pentane-CO<sub>2</sub>  
666 in the appropriate proportions was prepared and delivered to each sTGC with a gas system  
667 designed and made at McGill University [60]. Since pentane is flammable, the gas system  
668 was designed with safety top of mind. The gas system was controlled by a slow control  
669 program, also custom made [60]. To prepare the quadruplets for operation, CO<sub>2</sub> was flushed  
670 through them overnight to remove potential impurities within each chamber's gas volume.  
671 Then, the equivalent of approximately five sTGC gas volumes of the pentane-CO<sub>2</sub> mixture  
672 was flushed through to ensure a uniform gas mixture inside the sTGCs; the procedure takes  
673 approximately four hours. High voltage was provided by commercial CAEN high voltage  
674 boards [60].

## 675 5.3 Data acquisition

676 Each sTGC electrode was connected to a channel on a prototype ASIC<sup>1</sup> on the front-end elec-  
677 tronics, attached to the adaptor boards on each layer of a quadruplet. Each ASIC features  
678 64 charge amplifiers with selectable gain and input signal polarities, which output the digi-  
679 tized amplitude of the signal at peak for channels above a pre-defined threshold. Thresholds  
680 were estimated [62] by optimizing the efficiency of detecting muons while minimizing noise,  
681 and further manually tuned in the configuration/readout software before the start of data  
682 acquisition for each quadruplet. The signal from the capacitively-coupled strip electrodes  
683 has positive polarity and is read out with a gain of one. For each trigger, the signal peak  
684 amplitude of all channels above threshold was recorded as an event and stored in a binary  
685 file. The readout of strips made use of a special feature of the custom ASIC, the so-called  
686 “neighbour triggering” function where signals on channels adjacent to those above threshold  
687 are also read out.

688 The quadruplets were held at 3.1 kV for approximately two hours to collect data from  
689 approximately 1 million muon triggers.

---

<sup>1</sup>A custom Application Specific Integrated Circuit (ASIC) named VMM3 [61], designed for the readout of signals from the micromegas and sTGCs of the NSWs.

690 **5.4 Data preparation**

691 **5.4.1 Data quality cuts on electrode hits**

692 Corrupted data, if any, is removed while the raw data is being recorded in a binary file. After  
693 data taking is completed, the raw data is decoded and the electronics channels are mapped  
694 to physical readout electrodes of the quadruplet. The result of this data preparation step is  
695 stored in a ROOT [63] tree data format.

696 A hit is defined as a signal recorded from a channel that was above threshold or (in the  
697 case of strips) neighbour triggered. In addition to hits from muons, the quadruplets record  
698 noise from the electronics and  $\delta$ -rays (electrons liberated with sufficient energy to escape  
699 a significant distance away from the primary radiation and produce further ionization).  
700 Therefore, selection cuts are applied to reduce the number of hits that do not originate from  
701 muons. Readout strips located at the very edge of the cathode board tend to have higher  
702 electronic noise. As a result, all strip hits on a layer where a hit is present on the strips  
703 at either edge of the quadruplet are removed from the analysis. A default pedestal value  
704 is subtracted from the recorded signal peak amplitude of each electrode for a more realistic  
705 estimate of the signal amplitude. Also, events that only have hits on pad electrodes (no  
706 strips or wires) were removed from the analysis since these hits are likely from electronic  
707 noise, which is higher on the pad readout channels due to their large area.

708 **5.4.2 Clustering and tracking**

709 For events passing the quality selection cuts defined in section 5.4.1, the  $x$ - and  $y$ -coordinates  
710 of the ionization avalanche on each layer are extracted from the signal on the wires and strips  
711 respectively for each event, as shown schematically in figure 5.2. In this work,  $x$  is defined as  
712 the coordinate perpendicular to the wires and  $y$  is defined as the coordinate perpendicular  
713 to the strips. The  $z$ -coordinate is perpendicular to the sTGC surface.

714 The  $x$ -coordinate of the muon position is taken as the center of the wire group with the  
715 maximum peak signal amplitude, since the wire groups' pitch (36 mm) is larger than the  
716 typical extent of the ionization charge generated inside a sTGC. Assuming that the true  $x$ -  
717 position of the hit is sampled from a uniform distribution over the width of the wire group,  
718 the uncertainty in the  $x$ -position is approximately  $\frac{36}{\sqrt{12}}$  mm = 10 mm [64].

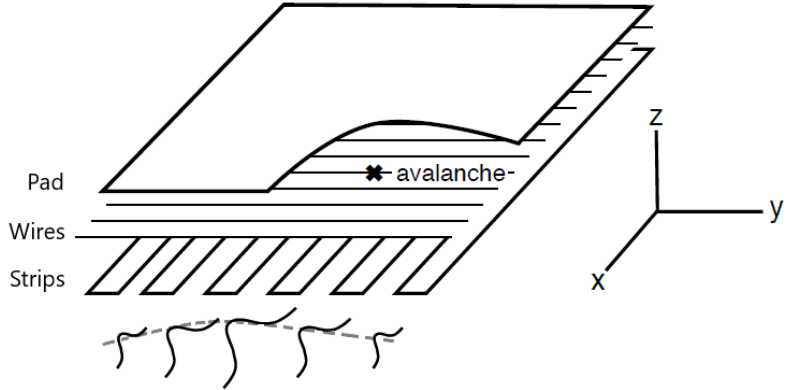


Figure 5.2: Schematic diagram representing the three types of electrodes in a sTGC detector. The position of the ionization avalanche is extracted from the wires and strips that picked up the avalanche signal. The signals on individual strips are sketched. Clustering is the process by which a Gaussian function (represented by the grey dashed line) is fitted to the distribution of the signal amplitude on individual contiguous strips; a sample cluster is shown in figure 5.3. In this work, the  $x(y)$ -coordinate will always refer to the coordinate perpendicular to the wires (strips). The  $z$ -coordinate is perpendicular to the sTGC surface [58, 56].

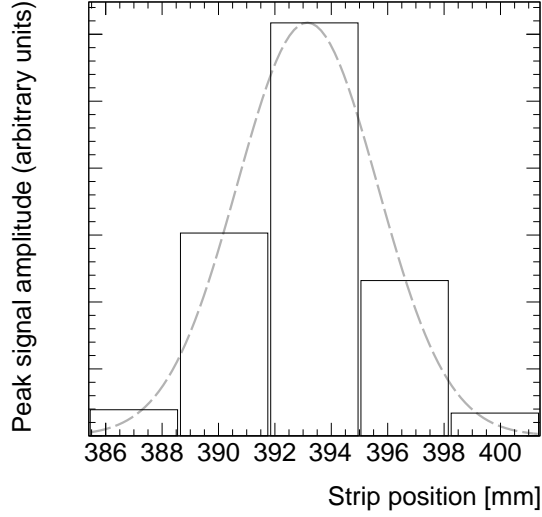


Figure 5.3: A sample cluster resulting from signal recorded on a group of contiguous strips after the passing of a muon. The grey dashed line represents the result of a fit to a Gaussian distribution.

719 The  $y$ -coordinate of the muon's position is taken as the Gaussian mean of the peak signal  
720 amplitude distribution across a group of contiguous strips that registered hits. The process  
721 of grouping contiguous strip hits on a layer is called clustering, and the resulting group is  
722 called a cluster. Figure 5.2 sketches the clustering process and a sample cluster is shown  
723 in figure 5.3. The data acquisition system recorded the identification number of the strip  
724 electrode that was hit and in the clustering process the position of the center of the strip  
725 electrode is calculated based on the nominal quadruplet geometry. Typically, clusters are  
726 built of 3-5 strips. The thickness of the graphite coating over the cathode boards determined  
727 how many strips picked up the ionization image charge. Larger clusters can often originate  
728 from  $\delta$ -rays since they spread the ionization charge over a larger area.

729 Events are removed from further analysis if there are two reconstructed clusters on one sTGC,  
730 since some hits could be from electronic noise or a simultaneous second muon traversing the  
731 chamber. Clusters are rejected if the cluster size is lesser than three strips (which should  
732 not happen for real events thanks to neighbour triggering), and if the cluster size is greater  
733 than 25. After all quality selection cuts are applied on hits and clusters, approximately half  
734 of the events recorded remain.

735 The uncertainty on the reconstructed cluster position is assessed by comparing the difference  
736 between Gaussian means obtained using two different algorithms. As shown in appendix A,  
737 the difference between the means from the two algorithms considered is found to be ap-  
738 proximately 60  $\mu\text{m}$  on average, larger than the statistical uncertainty on the Gaussian mean  
739 obtained from the cluster fit. Therefore, an uncertainty of 60  $\mu\text{m}$  is assigned to the recon-  
740 structed  $y$ -coordinate of a muon.

741 The reconstructed  $x$  and  $y$  coordinates on each quadruplet layer are used to reconstruct  
742 a straight track, independently, in the  $x$ - $z$  and  $y$ - $z$  planes. Tracks are reconstructed using  
743 muon coordinates for every possible pair of two sTGC layers. For example, if an event has  
744 muon coordinates reconstructed on all four layers, a total of six track segments in the  $x$ - $z$   
745 plane and six track segments in the  $y$ - $z$  plane will be reconstructed.

## 746 5.5 Relative local offsets

747 The offset of a strip from its nominal position can be modeled as a passive transformation.  
748 The *local offset* is defined as the shift in the strip pattern with respect to nominal geometry  
749 in a specific area of the sTGC. Local offsets systematically change the set of strips nearest  
750 to muons passing through an area. The data preparation software assumes that strips are  
751 in their nominal positions, so the recorded  $y$ -coordinate of the muon on layer  $i$ ,  $y_i$ , is shifted

752 opposite to the layer's local offset,  $d_{local,i}$ , by

$$y_i = y_{nom,i} - d_{local,i}, \quad (5.1)$$

753 where  $y_{nom,i}$  is the position of the muon that would have been recorded on layer  $i$  if there  
754 was no local offset. Equation 5.1 ignores other factors that affect the cluster position, like  
755 position resolution. With cosmics data, there was no external reference to measure  $y_{nom,i}$   
756 and the local offset is unknown. Therefore, only *relative* local offsets can be measured.

757 To measure relative local offsets, two of the four sTGC layers are chosen to provide a reference  
758 coordinate system. Relative local offsets are calculated with respect to the two reference  
759 or fixed layers. The hits on the two fixed layers were used to create tracks that can be  
760 interpolated or extrapolated (polated) to the other two layers. The set of two fixed layers  
761 and the layer polated to are referred to as a tracking combination. The residual of track  $i$ ,  
762  $\Delta_i$ , is defined as,

$$\Delta_i = y_i - y_{track,i}, \quad (5.2)$$

763 where  $y_{track,i}$  is the polated track position on the sTGC layer the residual is measured on.  
764 Track residuals are affected by the local offset in the area of each layer's hit. As an example,  
765 in figure 5.4, the residual on layer 2 perhaps indicates that layer 2 is offset with respect to  
766 layers 1 and 4 in the area of the track. Of course, a single track residual says nothing of  
767 the real relative local offset because of the limited spatial resolution of the detectors and  
768 fake tracks caused by noise or delta rays. However, the mean of residuals for all tracks in a  
769 region of interest will be shifted systematically by the local offsets between layers [58]. For  
770 a quadruplet with nominal geometry, the mean of residuals should be zero in all regions and  
771 for all reference frames, unlike the example regions in figure 5.5. The value of the mean of  
772 residuals is a measure of the relative local offset of the layer with respect to the two fixed  
773 layers used to reconstruct the muon track. The sign convention is such that the mean of  
774 residuals is opposite to the relative local offset.

775 To study the relative local offsets, residual distributions across each strip layer of a quadruplet  
776 for all possible tracking combinations are assembled and fitted. As expected, the residual dis-  
777 tributions are wider for tracking combinations where the extrapolation lever arm is largest,  
778 as in the example distributions shown in figure 5.5. In general, residual means from dis-  
779 tributions of residuals with geometrically less favourable tracking combinations have larger  
780 statistical and systematic uncertainties. The bin size of 200  $\mu\text{m}$  for the distributions shown  
781 in figure 5.5 was chosen based on the uncertainty on residuals calculated from tracks on layer  
782 4 (1) built from hits on layers 1 and 2 (3 and 4) given a cluster  $y$ -coordinate uncertainty  
783 of 60  $\mu\text{m}$  (discussed in section 5.4.2 and appendix A), since these tracks yield residuals with  
784 the largest uncertainties.

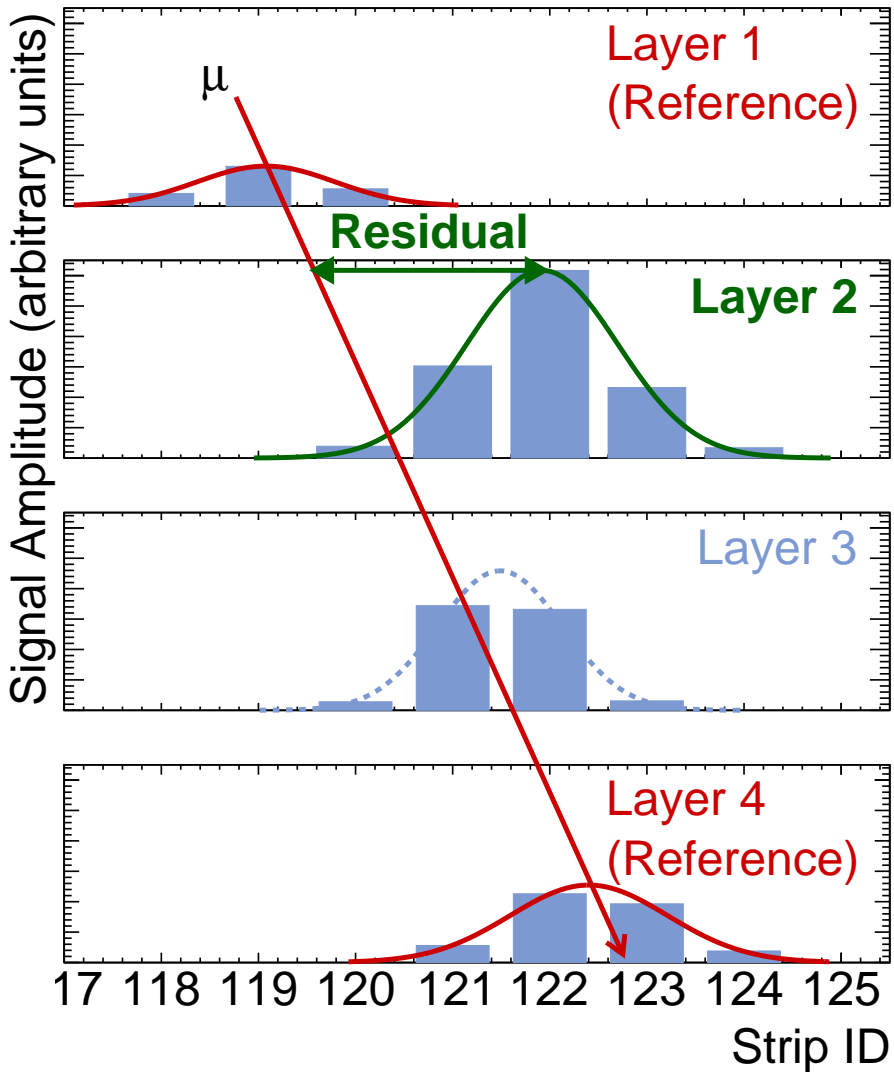
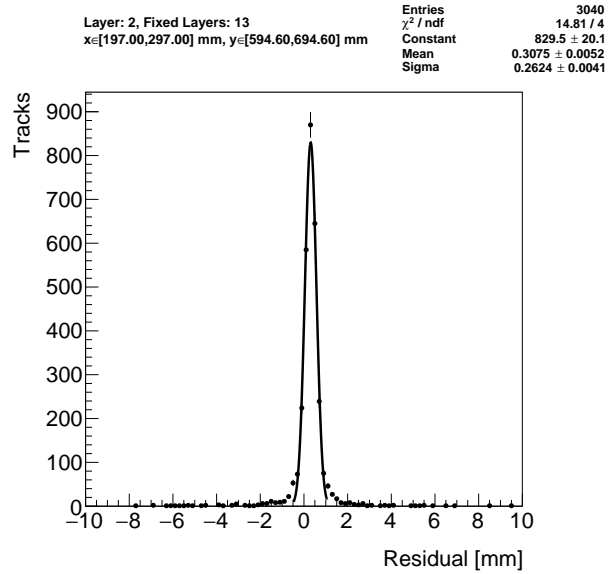
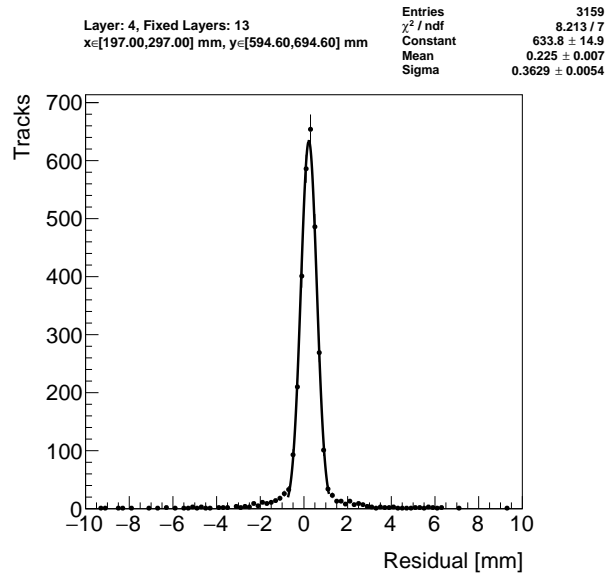


Figure 5.4: Representation of a muon event recorded by an sTGC quadruplet. The charge clusters measured using strip electrodes are fit with a Gaussian distribution and the fitted mean is taken as the reconstructed muon position. A track is built from the chosen reference layers, 1 and 4, and the track residual is calculated on layer 2. The clusters come from a real muon, but their positions were modified to highlight the non-zero value of the residual on layer 2.



(a) Tracks on layer 2, reference layers 1 and 3.



(b) Tracks on layer 4, reference layers 1 and 3.

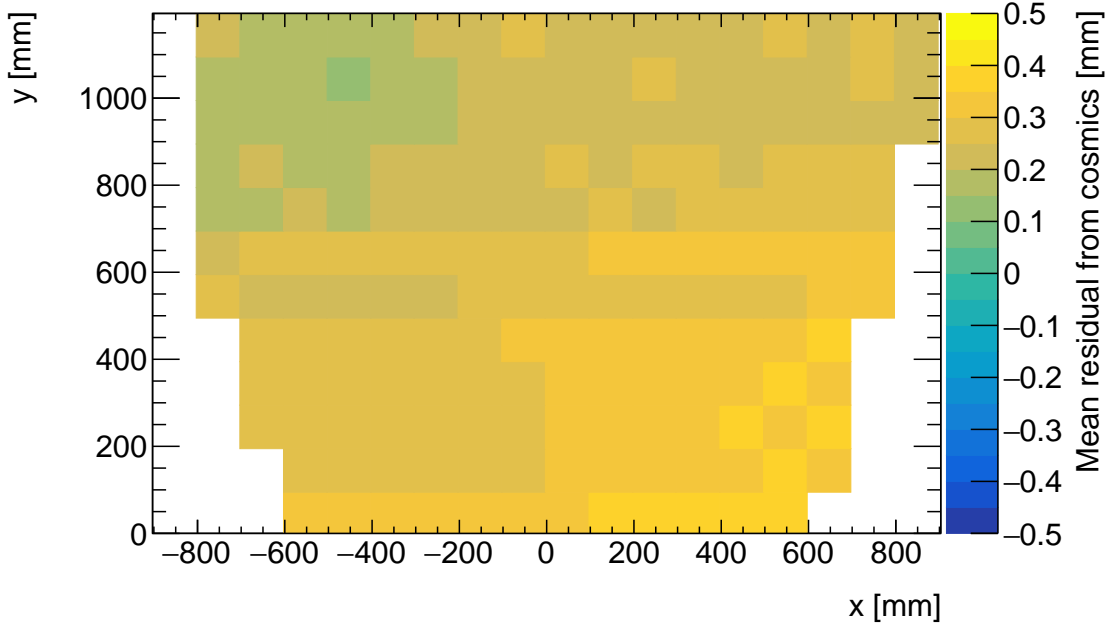
Figure 5.5: Residual distribution in the region  $x \in [197, 297]$  mm,  $y \in [594.6, 694.6]$  mm (100 mm by 100 mm area) for two different tracking combinations. Data from quadruplet QL2.P.11.

785 A Gaussian fit is used to extract the mean of the residual distributions. The residual distri-  
786 butions are actually better modeled by a double Gaussian distribution, which better captures  
787 the distribution tails in figure 5.5. However, a study described in appendix C.1 found that  
788 a fit to a single Gaussian function in the core of the distribution is sufficient to reconstruct  
789 the mean of the distribution.

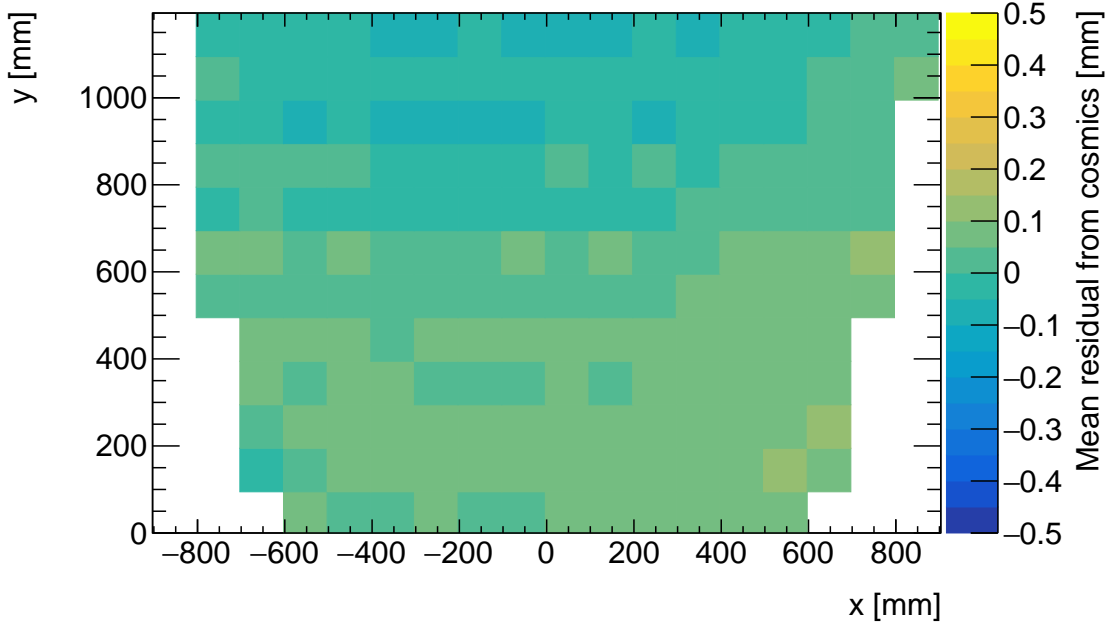
790 The area of the region of interest where tracks residuals were included in the residual distri-  
791 bution was 100 mm by 100 mm. The size balanced the number of tracks falling in the region  
792 of interest to give a small statistical uncertainty on the fitted mean while being smaller  
793 than the order on which local offsets were expected to change significantly. “Significantly”  
794 was defined as 100  $\mu\text{m}$ , the required position resolution of the sTGCs and the precision to  
795 which strip positions should be known. The distance over which local offsets are expected to  
796 change significantly can be estimated using a simple alignment model. Assuming the strips  
797 of a layer have been displaced uniformly from their nominal positions by a global offset and  
798 rotation, the distance in  $x$  that a large but possible rotation of 1 mrad changes the local  
799 offset by 100  $\mu\text{m}$  is 100 mm.

800 The means of residuals are plotted across each sTGC layer for every possible tracking combi-  
801 nation to get a picture of the how the relative local offsets change as a function of position  
802 over the layer’s surface. Figure 5.6 shows the mean of residuals on layer 2 calculated with  
803 layers 1 and 3 as reference for two different quadruplets, referred to as QL2.P.11 and QL2.P.8.  
804 In figure 5.6a, the Gaussian mean of the residual distribution in figure 5.5a is the entry in  
805 the bin defined by the boundaries  $x \in [197, 297]$  mm,  $y \in [594.6, 694.6]$  mm.

806 Many of the residual means are non-zero and change smoothly over layer 2, indicating that  
807 there are relative local offsets stemming from global misalignments between the strip patterns  
808 of different sTGC layers in both quadruplets. Given that the residual mean changes with  $x$  in  
809 figure 5.6a, quadruplet QL2.P.11 likely has a rotation of layer 2 with respect to layers 1 and  
810 3, combined with an offset of the entire layer. The residual means are smaller in figure 5.6b  
811 indicating that quadruplet QL2.P.8 is less misaligned overall than QL2.P.11; however, the  
812 relative local offsets range between  $\pm 200 \mu\text{m}$  so they are significant enough to warrant a  
813 correction so the quadruplet can achieve the required track angular resolution in the NSW.



(a) Mean of track residuals on layer 2, obtained using layers 1 and 3 as reference, for QL2.P.11.



(b) Mean of track residuals on layer 2, obtained using layers 1 and 3 as reference, for QL2.P.8.

Figure 5.6: Mean of residuals in each 100 mm by 100 mm bin over the area of sTGC layer 2 for quadruplets QL2.P.11 and QL2.P.8. The entry in  $x \in [197, 297]$  mm,  $y \in [594.6, 694.6]$  mm of figure 5.6a corresponds to the fitted Gaussian mean in figures 5.5a. The mean of residuals has the same value and opposite sign to the relative local offset of layer 2 with respect to the reference frame defined by layers 1 and 3.

## 814 5.6 Systematic uncertainty

815 The statistical uncertainty on the local residual means was typically around 10 - 20  $\mu\text{m}$ , and  
816 appendix B shows that the analysis is not statistically limited by the number of triggers  
817 collected for each quadruplet. Systematic uncertainties were found to be larger than the  
818 statistical uncertainty on the residual means.

819 Several analysis choices had some degree of impact on the fitted means of local track residual  
820 distributions. To study the impacts, the residual means were calculated in different ways and  
821 distributions of the differences made. The complete studies are shown in appendix C. The  
822 root-mean-square (RMS) of the residual mean difference distributions were used to quantify  
823 the impact of the different analysis choices as systematic uncertainties on the residual means.  
824 The following analysis choices are considered:

- 825 • The impact of performing a single or double Gaussian fit on the track residual distri-  
826 butions is studied. As shown in appendix C.1, the difference between fitting the track  
827 residual distribution with a single or double Gaussian function varies between 10-30  $\mu\text{m}$   
828 from the most to least geometrically favourable tracking combinations.
- 829 • The impact of the operating voltage used during data taking is investigated. Cosmic  
830 muon data was recorded at 2.9 kV and 3.1 kV. As described in appendix C.2, an  
831 uncertainty between 10-40  $\mu\text{m}$  is assigned to the different tracking combinations.
- 832 • The impact of using different Gaussian fitting algorithms used to reconstruct the po-  
833 sition of a charge cluster was considered. Clusters are fit with the Minuit2 [65] and  
834 Guo's method [66]. As shown in appendix C.3, the resulting difference in residual  
835 means is between 10-30  $\mu\text{m}$  from the most to least geometrically favourable tracking  
836 combinations.
- 837 • The impact of correcting reconstructed cluster positions for differential non-linearity  
838 (DNL) is studied. DNL is fully described in appendix C.4. It is a bias in the recon-  
839 structed cluster position that comes from discretely sampling a continuous distribu-  
840 tion, in this case the charge distribution [67, 58, 6]. The difference between residual  
841 means is compared with and without correcting the reconstructed cluster positions.  
842 Appendix C.4 shows that the impact of the correction is smaller than 10  $\mu\text{m}$  for all  
843 tracking combinations, which is almost negligible.

844 A summary of the systematic uncertainties assigned to the local means of residuals for each  
845 tracking combination is given in table 5.1. The RMS of the distributions of residual mean  
846 differences of geometrically similar tracking combinations are averaged and the average value

Tracking geometry	Residual distribution fit function (C.1)	Cosmics data collection voltage (C.2)	Cluster fit algorithm (C.3)	Apply DNL correction or not (C.4)	Total
Similar to layer 3, fixed layers 1, 2	0.01 mm	0.04 mm	0.02 mm	0.01 mm	<b>0.05 mm</b>
Similar to layer 4, fixed layers 1, 2	0.03 mm	0.01 mm	0.03 mm	0.01 mm	<b>0.10 mm</b>
Similar to layer 2, fixed layers 1, 3	0.01 mm	0.02 mm	0.01 mm	0.000 mm	<b>0.03 mm</b>
Similar to layer 4, fixed layers 1, 3	0.01 mm	0.04 mm	0.01 mm	0.01 mm	<b>0.04 mm</b>
Similar to layer 2, fixed layers 1, 4	0.01 mm	0.04 mm	0.01 mm	0.01 mm	<b>0.04 mm</b>

Table 5.1: Systematic uncertainty assigned for each analysis option, detailed in appendix C.

847 is taken as the systematic uncertainty for those tracking combinations. An example of a ge-  
 848 ometically similar pair of tracking combinations is fixing layers 1 and 2 and extrapolating  
 849 to layer 3 or fixing layers 2 and 3 and extrapolating to layer 4; geometrically similar combi-  
 850 nations have the same polation lever arm. The total systematic uncertainty is obtained by  
 851 summing in quadrature all the different sources of systematic uncertainty. The uncertainty  
 852 in each mean of residuals is obtained by summing in quadrature the statistical uncertainty  
 853 in the mean of residuals and the appropriate systematic uncertainty for the tracking com-  
 854 bination used to calculate the mean of residuals.

## 855 5.7 Discussion

856 The total uncertainty in the residual means, and hence the relative local offsets, is typically  
 857 less than the design sTGC position resolution of  $\sim 100 \mu\text{m}$  [5]. Therefore, the residual means  
 858 are relevant input for alignment studies.

859 The relative local offsets calculated from the means of residual distributions over the surface  
860 of an sTGC layer for all tracking combinations provide a complete picture of the relative  
861 alignment between sTGC layers in a quadruplet module. In fact, cosmic muon testing is the  
862 only characterization technique where the entire surface of quadruplet layers can be probed  
863 since muons hits are distributed almost uniformly; the CMM [7] and x-ray methods [8]  
864 depend on measurements at reference points, and test beams only have a limited beam spot  
865 to work with [6]. By looking at 2D-histograms of residual means like figure 5.6 for all tracking  
866 combinations, it is easy to identify quadruplets that suffer large relative misalignment since  
867 many residual means differ significantly from zero. Moreover, the pattern in the residual  
868 means can be used to motivate a physical interpretation of misalignments. The residual  
869 means can be used as a reference, cross check, or input to other alignment studies.  
870 Relative local offsets cannot be used to position strips in the absolute ATLAS coordinate  
871 system because there is no external reference to measure positions on all layers with respect  
872 to. The lack of an external absolute reference frame means that there is not enough infor-  
873 mation to unfold relative local offsets into absolute local offsets (with respect to the nominal  
874 quadruplet geometry). As an example, assuming that the residual on layer 2 in figure 5.4 is  
875 representative of the absolute value of the relative local offset, the residual on layer 2 could  
876 be caused by the strips on layer 2 being misaligned from nominal, but it could also be caused  
877 by strips on layers 1 and 4 being offset from nominal while the strips on layer 2 are in their  
878 nominal positions! Any number of combinations of local offsets on layers 1, 2 and 4 could  
879 produce the residual on layer 2. Absolute local offsets must be calculated using another  
880 method: the x-ray method.

881 **Chapter 6**

882 **Using x-rays to measure relative strip  
883 position offsets**

884 This chapter describes the analysis of x-ray data to measure relative local strip position  
885 offsets, which can be compared with results obtained using cosmic data. The reader is re-  
886 ferred to the paper describing the x-ray method [8]. Some minor changes to the experimental  
887 setup have been made since the paper was written. The experimental setup described here  
888 is current and was used to collect the data presented in this thesis.

889 **6.1 Experimental setup**

890 The x-ray tests were performed after the quadruplets had arrived at CERN, had been were  
891 assembled into wedges, and the alignment platforms installed. An x-ray gun was attached to  
892 one of the alignment platforms glued to the surface of the wedge and the x-ray beam profile  
893 was recorded by the strip electrodes.

894 The sTGC wedges were installed on carts that could rotate their surface to a horizontal  
895 position. A mounting platform was installed on top of the alignment platform using a three-  
896 ball mount. The x-ray gun used was an Amptek Mini-X tube [68]. The x-ray gun was placed  
897 in a brass holder with built-in 2 mm collimator and 280  $\mu\text{m}$  copper filter. The holder was  
898 mounted on one of five positions on the mounting platform, as shown in figure 6.1. The  
899 x-ray gun positions were chosen to avoid wire support structures in the sTGCs that reduce  
900 hit efficiency [58] and boundaries between sets of strips read out by two different ASICs that  
901 could each have different thresholds.

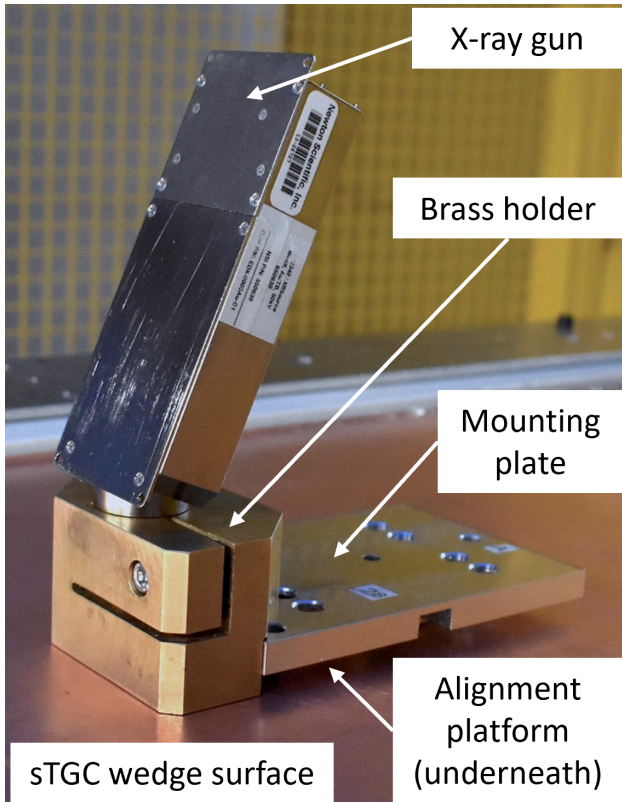


Figure 6.1: The x-ray gun mounted to an alignment platform on the surface of a sTGC wedge. Adapted from [8].

- 902 As with cosmics data collection, each sTGC also needed gas and high voltage to operate.  
 903 Each sTGC layer was operated at 2.925 kV with high voltage from a NIM crate. The sTGC  
 904 gas volumes were flushed with CO<sub>2</sub> before and during data collection. The sTGCs were not  
 905 operated using the nominal pentane-CO<sub>2</sub> gas mixture due to constraints in its availability  
 906 based on safety concerns. The sTGC efficiency is significantly lower when operated with  
 907 only CO<sub>2</sub>.  
 908 The gun produced x-rays with energies under 40 keV with peaks in the 7-15 keV range. Peaks  
 909 in the 0-30 keV range were filtered out by the copper filter and the copper of the sTGCs. The  
 910 x-rays mostly interacted with the sTGC wedge's copper electrodes and gold-plated tungsten  
 911 wires via the photoelectric effect. The resulting photoelectrons that enter the gas volume  
 912 caused ionization avalanches which were picked up by the readout strips.

913 **6.2 Data acquisition**

914 A different version of the same front end electronics, but the same ASIC, as used in cosmics  
915 testing were used for the x-ray testing to measure the peak signal amplitude. Data was  
916 collected for two minutes per gun position with random triggers. A trigger recorded all  
917 signals above threshold. Pad and wire data was not recorded.

918 **6.3 Data preparation**

919 Following a similar approach to the cosmics data analysis described in chapter 5, a default  
920 pedestal is subtracted from the signal peak amplitude on each electrode.

921 Clusters are defined as groups of contiguous strip hits recorded within 75 ns. The distribution  
922 of peak signal amplitude from continuous strip hits is fitted with a Gaussian function, and the  
923 mean of the fitted Gaussian is taken as the cluster position. Cluster positions are corrected  
924 for differential non linearity (or DNL, see definition in appendix C.4). Although the impact  
925 of the DNL correction on the reconstructed cluster means is small, it is important to improve  
926 the spatial resolution of the sTGC strip layer. Only clusters composed of hits on 3-5 strips  
927 are used in the x-ray analysis. Clusters with signal on more than five strips are cut because  
928 they were most likely caused by photoelectrons ejected with enough energy to cause more  
929 primary ionization and subsequent avalanches as  $\delta$ -rays.

930 The x-ray analysis diverges entirely from the cosmics analysis algorithm here because the  
931 ionization from x-rays does not originate from one charged particle traversing all layers  
932 of a sTGC quadruplet, so there is no track to rebuild. Rather, ionization avalanches [54]  
933 are generated by photoelectrons liberated from the metals of the sTGCs, which only travel  
934 through one gas volume and are produced at all angles. Instead of reconstructing a straight  
935 line trajectory through multiple sTGC layers, the cluster position distribution on each sTGC  
936 layer is used to reconstruct the beam profile. A typical x-ray beam profile is shown in  
937 figure 6.2.

938 **6.4 Measuring local offsets**

939 The fitted Gaussian mean of the cluster position distribution is taken as the reconstructed  
940 center of the x-ray beam profile on each sTGC layer. The reconstructed center is compared to  
941 the expected beam profile center, calculated in two steps. First, the position of the alignment  
942 platform with respect to the brass inserts and the nominal position of the strips under the

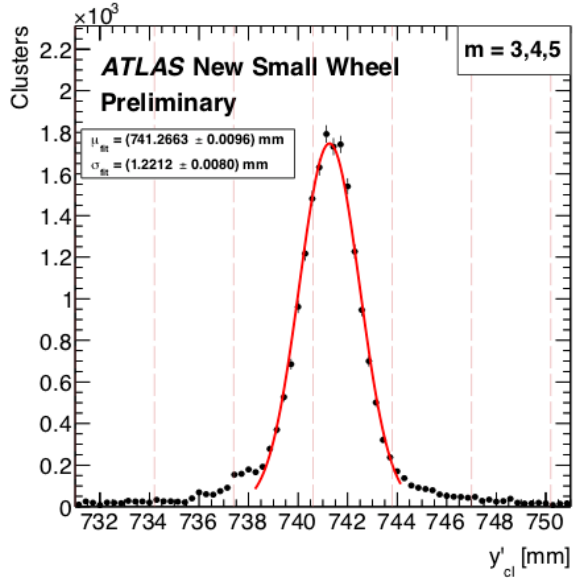


Figure 6.2: An example distribution of x-ray cluster mean positions after the analysis selection cuts and DNL corrections are applied. The strip cluster multiplicity,  $m$ , was limited to 3, 4 or 5. The red curve is a Gaussian fit of the distribution and the pink dashed lines denote the edges of the strips [8].

943 gun position with respect to the brass inserts are used to calculate the expected beam profile  
 944 center assuming a nominal quadruplet geometry. Second, the expected beam profile center  
 945 is corrected for the geometry of the brass holder, the positioning and angle of the alignment  
 946 platforms, and the beam angle. The difference between the expected and reconstructed beam  
 947 profile centers is a measure of the local offset of the strip electrode pattern. Applying the  
 948 logic of equation 5.1 to the beam profile, the Gaussian mean of cluster positions on the given  
 949 layer acts as the recorded position,  $y_i$ , the expected center is  $y_{nom,i}$  and the local offset is  
 950  $d_{local,i}$  as before, where  $i$  denotes the layer. Since the position of the alignment platforms will  
 951 be monitored continuously by the alignment system in ATLAS [5], the position of the strips  
 952 that should have been at the x-ray gun position are shifted by  $d_{local,i}$  and so their absolute  
 953 positions in the ATLAS coordinate system are known for every position where x-ray data  
 954 was recorded. Therefore, the x-ray local offsets can be used to measure the position of  
 955 some strips in the ATLAS coordinate system, as is required for the triggering and precision  
 956 tracking goals of the NSWs as discussed in chapter 4.

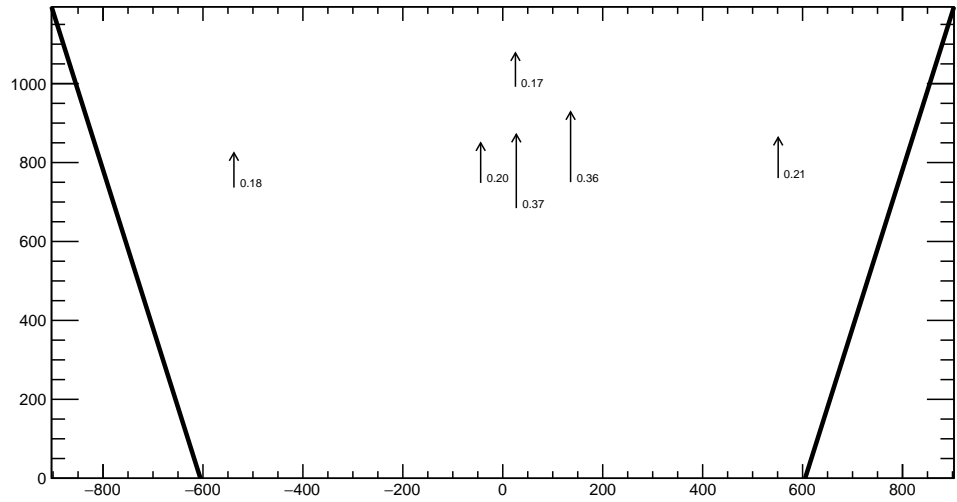
957 Studies of systematic effects on the measured beam profile centers lead the x-ray working  
 958 group to accept an uncertainty of 120  $\mu\text{m}$  on the beam profile centers. The largest uncertainty

959 comes from the effect of the gun angle, which proved difficult to measure and correct for.  
960 The details and results of the systematics studies have not been published externally.  
961 The absolute local strip offsets measured using the method described above are not presented  
962 here as the author did not conduct this work. However, the author used the *absolute* local  
963 offsets to calculate *relative* local offsets that can be compared to the relative local offsets  
964 measured using cosmic muon data.

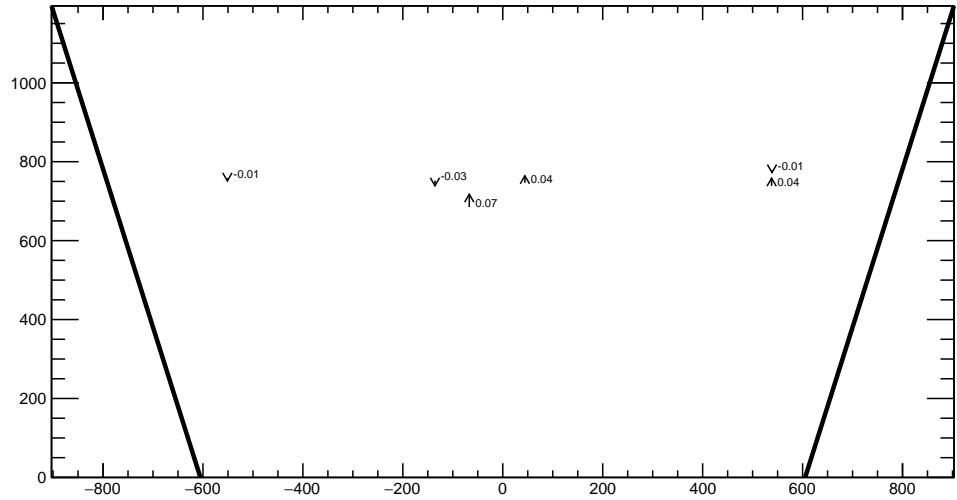
## 965 6.5 Measuring relative local offsets

966 The novelty of the x-ray method and the uncertainty in the x-ray local strip position offsets,  
967 which greater than the precision to within which the position of the strips would ideally be  
968 known, means that the x-ray local offsets should be validated by an independent method.  
969 Absolute local offsets measured using x-ray data and relative local offsets measured using  
970 cosmics data cannot be compared directly because they are not defined with respect to the  
971 same coordinate system: x-ray absolute local offsets are measured in the ATLAS coordinate  
972 system while cosmics relative local offsets are defined with respect to a reference frame  
973 established by two sTGC layers in a quadruplet. The following describes the method used to  
974 calculate relative local strip position offsets from the x-ray local offsets that can be compared  
975 to the cosmics relative strip position offsets.

976 Given that the measured x-ray beam profile centers are systematically affected by local strip  
977 position offsets in the same way as the means of the cosmic ray track residual distributions,  
978 the x-ray beam profile centers on each sTGC layer are used to reconstruct a straight line in  
979 the  $y$ - $z$  plane using the beam profile centers on two sTGC layers chosen as reference, in a  
980 manner similar to the track reconstruction performed with cosmic muon data. A residual  
981 is calculated as the difference between the beam profile center on the layer of interest and  
982 the polated straight line fitted from two sTGC layers taken as a reference. The beam profile  
983 center on the layer of interest acts as  $y_i$  and the polated track position acts as  $y_{track,i}$  in  
984 equation 5.2. As with the means of cosmic track residual distributions, the sign convention  
985 is such that the x-ray residual is opposite in sign to the relative local offset of the layer of  
986 interest with respect to the two fixed layers.



(a) X-ray residuals on quadruplet QL2.P.11 layer 2 obtained using reference layers 1 and 3.



(b) X-ray residuals on quadruplet QL2.P.8 layer 2 obtained using reference layers 1 and 3.

Figure 6.3: The x-ray residuals on sTGC layer 2 calculated with respect to the beam profile centers on sTGC layers 1 and 3 for quadruplet QL2.P.11 (a) and QL2.P.8 (b). The arrows originate from the expected position of the beam profile center assuming a nominal geometry. The lengths of the arrows are 500 times the value of the x-ray residuals, scaled for visibility. The value of the x-ray residuals are annotated in millimeters and have an uncertainty of  $\pm 0.15$  mm.

987 For each x-ray survey position, the x-ray residuals were calculated for all possible pairs of  
988 sTGC layers taken as reference and each sTGC layer the straight line could be polated to, as  
989 was done for cosmic muon tracks. Calculating a residual required x-ray beam profiles on at  
990 least three layers. Figure 6.3 shows the x-ray residual values on sTGC layer 2 with respect to  
991 reference layers 1 and 3 for sTGC quadruplet modules QL2.P.11 and QL2.P.8. For module  
992 QL2.P.11, a negative relative local offset is measured at all x-ray survey points, indicating a  
993 global translation of sTGC layer 2 with respect to layers 1 and 3.  
994 The uncertainty on the x-ray residualsis is obtained by propagating the uncertainty on the  
995 reconstructed x-ray beam profile centers ( $120\text{ }\mu\text{m}$ ) through the polation. The uncertainty  
996 on the x-ray residuals ranges from  $150\text{ }\mu\text{m}$  to  $400\text{ }\mu\text{m}$  from the most to least geometrically-  
997 favourable tracking combination. There is no discernible pattern of misalignmnet revealed by  
998 the x-ray residuals on QL2.P.8 because they have absolute values smaller than the uncertainty  
999 on the x-ray residuals ( $150\text{ }\mu\text{m}$ ).  
1000 The relative local offsets calculated using cosmics data and x-ray data will be compared in  
1001 the next chapter.

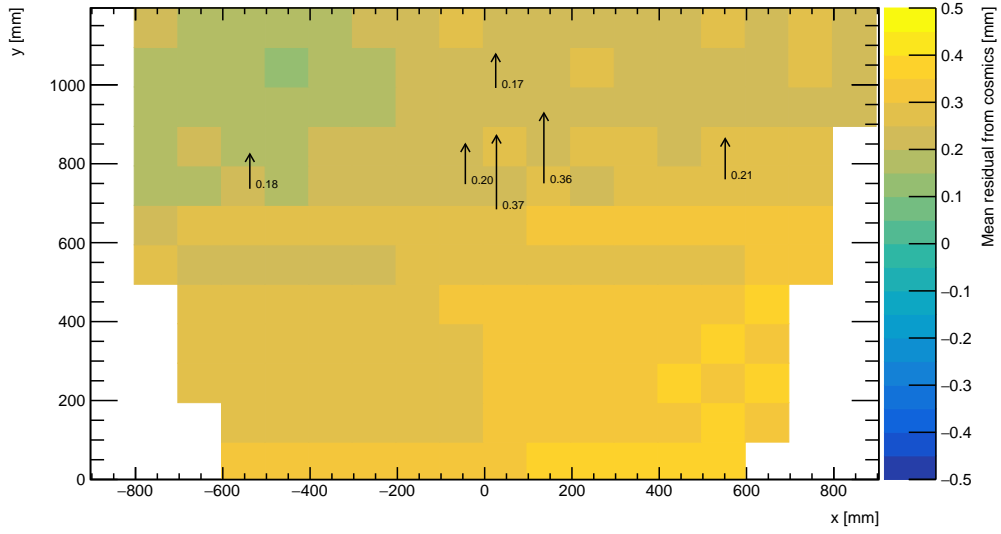
# 1002 Chapter 7

## 1003 Comparing cosmic muon and x-ray 1004 relative strip position offsets

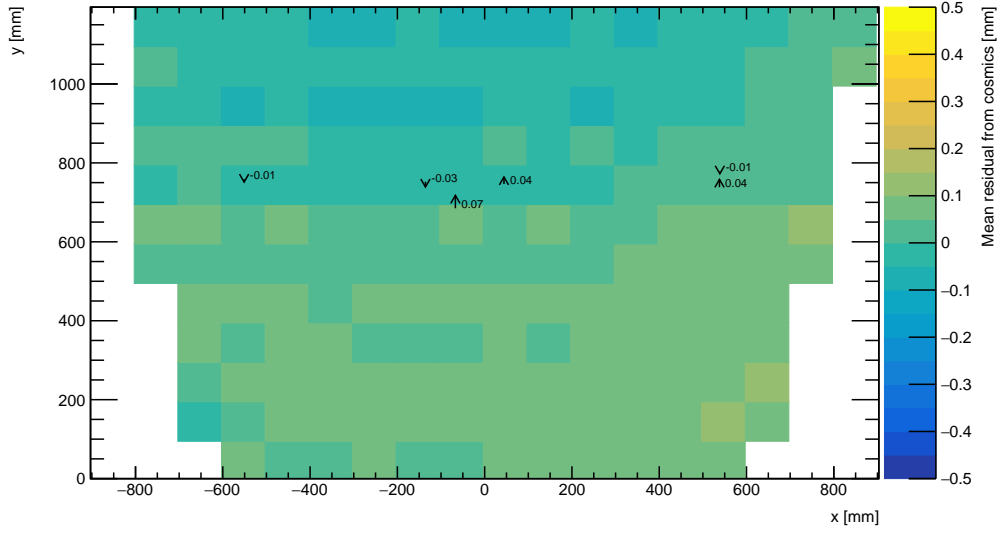
1005 The goal of the work presented in this thesis is to validate the local strip position offsets  
1006 measured with x-ray data with results obtained using cosmic ray data. The challenge was  
1007 that the x-ray dataset provided absolute local offsets measured in the ATLAS coordinate  
1008 system while the cosmics dataset provided relative local offsets measured with respect to a  
1009 reference frame defined by two of four sTGC layers in a quadruplet – which could not be  
1010 compared directly. To address the challenge, the x-ray local offsets were used to calculate  
1011 relative local offsets. Relative local offsets on each sTGC layer obtained with x-ray and  
1012 cosmics data calculated using the same two sTGC reference layers are compared for each  
1013 area where x-ray data is available. The results of the comparison are presented here.

### 1014 7.1 Results

1015 Relative local offsets have the same value but opposite sign to the mean cosmics and x-ray  
1016 residuals. For the remainder of this chapter, the means of cosmic track residual distributions  
1017 will be referred to as mean cosmics residuals.  
1018 Mean cosmics and x-ray residuals on sTGC layer 2 calculated with reference layers 1 and 3  
1019 across the quadruplet surface are shown in figure 7.1 for sTGC quadruplets QL2.P.11 and  
1020 QL2.P.8. Figure 7.1 is a superposition of figures 5.6 and 6.3.



(a) Mean cosmics and x-ray residuals on sTGC layer 2 of quadruplet QL2.P.11 obtained using reference layers 1 and 3.



(b) Means cosmics and x-ray residuals on sTGC layer 2 of quadruplet QL2.P.8 obtained using reference layers 1 and 3.

Figure 7.1: The mean cosmics residuals are shown using colour. The x-ray residuals available at nominal gun positions are drawn as arrows and the value of the residual annotated in millimeters with uncertainty  $\pm 0.15$  mm. The length of the arrows is 500 times the value of the x-ray residual, scaled for visibility. These plots are a superposition of figures 5.6 and 6.3.

1021 Figure 7.1a shows that for QL2.P.11 the x-ray residuals are of the same sign and order as  
1022 the mean cosmics residuals, as can be seen by comparing the annotated value of the x-ray  
1023 residual to the mean cosmics residual represented in the nearest coloured bin. QL2.P.11's  
1024 mean cosmics and x-ray residuals are correlated.

1025 For QL2.P.8, figure 7.1b shows that the x-ray residuals are of the right order compared to the  
1026 mean cosmics residuals; however, the value of the x-ray residuals are within their uncertainty  
1027 so the correlation is not manifest. While the x-ray residuals do not reveal a pattern in the  
1028 relative local offsets across the layer's surface, the mean cosmics residuals show a structure  
1029 to the relative local offsets, revealed by how they vary smoothly over the surface of sTGC  
1030 layer 2.

1031 The comparison of mean cosmics and x-ray residuals was done for several sTGC quadruplets  
1032 for all possible tracking combinations. Scatter plots of the x-ray and mean cosmics residuals  
1033 on QL2.P.11 and QL2.P.8 for all tracking combinations are shown in figures 7.2 and 7.3  
1034 and reveal the degree of correlation between the datasets. In these correlation plots, each  
1035 rectangle is centered on the value of a mean cosmics and x-ray residual pair calculated with a  
1036 given tracking combination for every x-ray gun position where data is available. The height  
1037 and width of the rectangles are the uncertainty in the mean cosmics and x-ray residuals  
1038 respectively. Note that in the scatter plots, the regions of interest where cosmics tracks are  
1039 included in the calculation of the mean of residuals are exactly centered on the nominal x-ray  
1040 beam positions, unlike in figure 7.1.

1041 The fitted slope and offset in figure 7.2 show that the two QL2.P.11 datasets are correlated.  
1042 The large uncertainty on the x-ray residuals set a limit on the sensitivity of the analysis,  
1043 for if the absolute value of the x-ray residuals of a quadruplet were smaller than the x-ray  
1044 residual uncertainties, no conclusion about the correlation could be drawn, as is the case for  
1045 layer 2 of sTGC quadruplet QL2.P.8 (figure 7.3). This result is reflected in the small x-ray  
1046 residuals shown in figure 7.1b that do not reveal a pattern in the relative local offsets across  
1047 the surface of sTGC layer 2. However, figure 7.3 shows that the x-ray and mean cosmics  
1048 residuals are clustered approximately around zero as is expected for a quadruplet with small  
1049 relative misalignments between layers.

1050 There are three patterns in the residuals on the scatter plot explained by geometry. First,  
1051 for both datasets the uncertainty in the extrapolated track residuals were larger than the  
1052 interpolated track residuals because of the extrapolation lever arm. For the x-ray residuals,  
1053 the effect of the lever arm on the uncertainty was direct since the residual was calculated  
1054 from a single straight line; for the mean cosmics residuals it is the widening of the residual  
1055 distributions due to the extrapolation lever arm that increases the uncertainty in the fitted  
1056 means of residuals. Second, residuals calculated through extrapolation tend to be larger  
1057 because the extrapolation lever arm can produce more extreme values of the track position

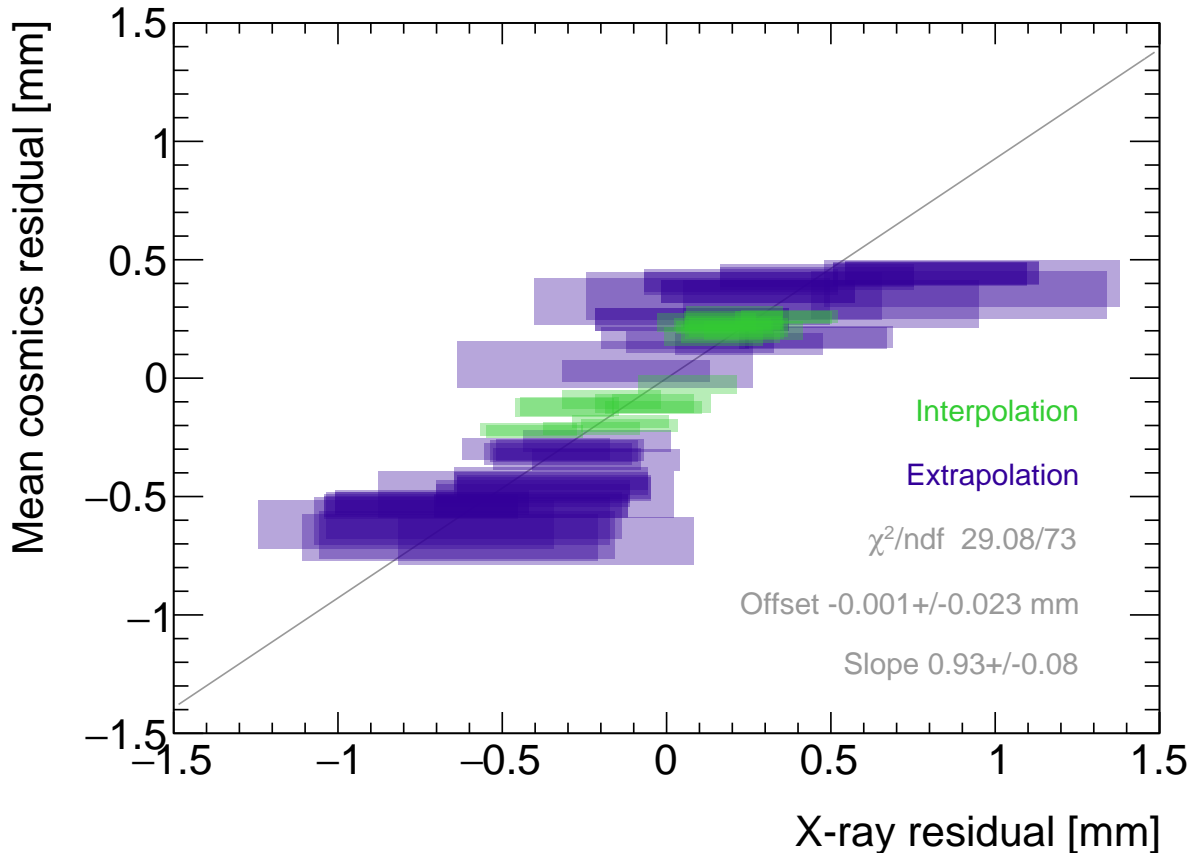


Figure 7.2: Correlation plot between x-ray and mean cosmics residuals for all tracking combinations for QL2.P.11. Each rectangle is centered on an x-ray and mean cosmics residual pair calculated at a given x-ray gun position and for a certain tracking combination. The width of the rectangles in  $x$  and  $y$  are the uncertainty in the x-ray and mean cosmics residual respectively. A printer-friendly version of this plot is available in appendix D.

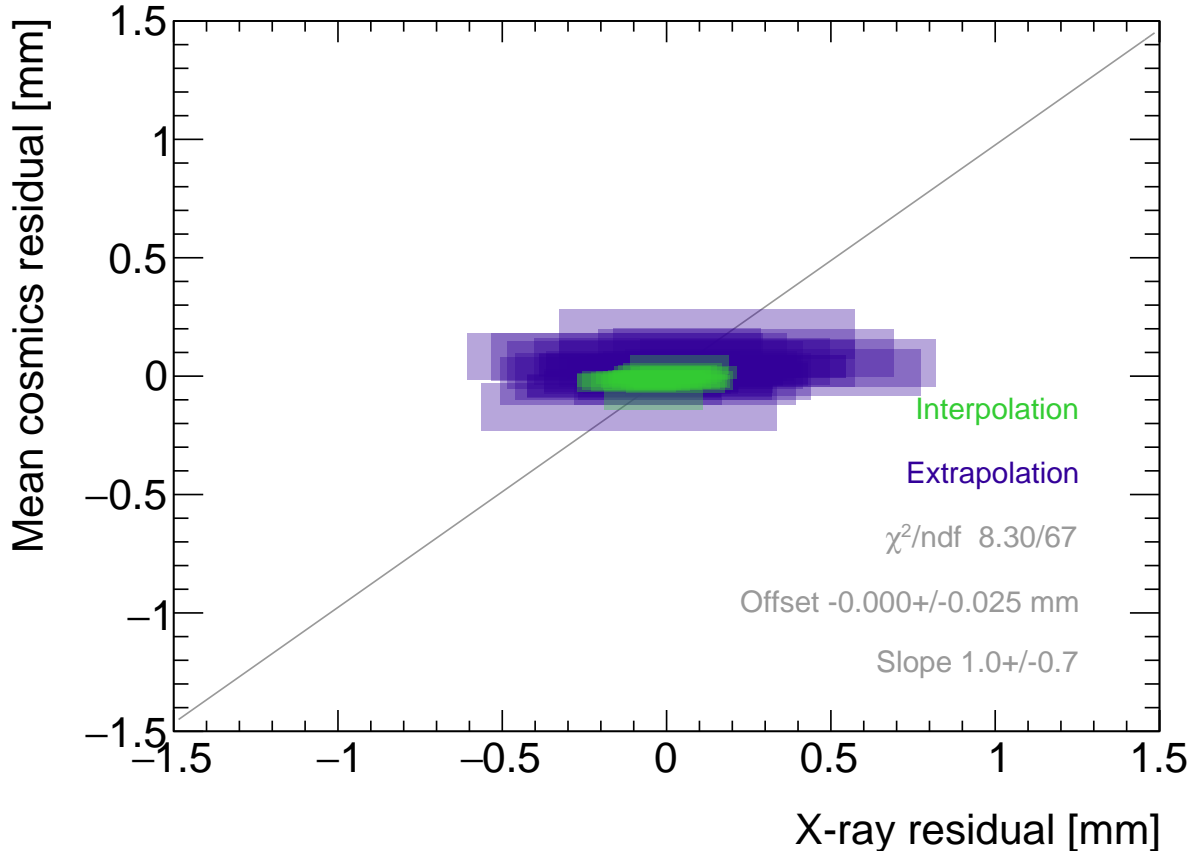


Figure 7.3: Correlation plot between x-ray and mean cosmics residuals for all tracking combinations for QL2.P.8. Each rectangle is centered on an x-ray and mean cosmics residual pair calculated at a given x-ray gun position and for a certain tracking combination. The width of the rectangles in  $x$  and  $y$  are the uncertainty in the x-ray and mean cosmics residuals respectively. A printer-friendly version of this plot is available in appendix D.

on the layer of interest. Third, the points in figure 7.2 are geometrically correlated (e.g. they seem to be roughly mirrored around the origin). This is expected since the residuals calculated using a given set of three layers should be geometrically correlated by the local offsets on each layer (the  $d_{local,i}$  on each layer as defined in equation 5.1).

## 7.2 Discussion

Several sTGC quadruplets were tested for each quadruplet construction geometry built in Canada. Each quadruplet fell into one of the two categories: residuals large enough to see a correlation, or residuals too small to see a correlation. Since the x-ray and mean cosmics residuals can be used to calculate relative local offsets between the layer and the two reference layers, quadruplets with the largest relative misalignments had the largest range of residuals. The correlation plots are another easy visual way to identify quadruplets with large relative misalignments.

The most significant limit on measuring the degree of correlation between the x-ray and mean cosmics residuals is the uncertainty on the x-ray residuals, which stemmed from the systematic uncertainty of 120  $\mu\text{m}$  in the x-ray beam profile centers used to construct the straight lines. For example, in figure 7.3, if the x-ray residuals could be known to within better precision, perhaps they would be correlated with the mean cosmics residuals. The x-ray method was limited primarily by the systematic uncertainties in the relative alignment of the alignment platforms and the gun, especially the gun angle.

The analysis of a fraction of the sTGC quadruplets was limited by the availability of data. Sometimes, less than three sTGC layers in a quadruplet were surveyed for a given x-ray gun position so no residuals could be calculated. Too few x-ray residuals prevented the analysis from detecting a significant correlation with cosmics data, should it even be measurable. Often, the analysis of sTGC quadruplets of smaller sizes (placed innermost on the wheel) is limited because they have fewer alignment platforms, and hence gun positions, on their surfaces as a result of their size. The analysis is also limited to a fraction of all sTGC quadruplets built. The wedges constructed the earliest (typically small wedges) were surveyed when the x-ray method was still being designed, so a limited number of x-ray residuals can be calculated and the beam profiles were of lower quality.

Nonetheless, the comparison of x-ray and mean cosmics residuals was really to confirm the x-ray method's ability to measure local offsets with an independent dataset. The x-ray local offsets allow the calculation of relative local offsets that have been correlated to the cosmics relative local offsets. Therefore, the analysis of quadruplets with relative local offsets large enough to detect a correlation validates the x-ray method's ability to measure local offsets.

1092 The potential of using relative local offsets calculated from cosmics data to study relative  
1093 alignment between sTGC layers stands on its own. For example, although the x-ray residuals  
1094 in QL2.P.8 in figure 7.1b do not reveal a pattern, the variation in the mean cosmics residuals  
1095 do. Identifying the pattern is possible because mean cosmics residuals can be calculated  
1096 across the entire sTGC layer's area and are sensitive to smaller relative local offsets since  
1097 their uncertainty is significantly smaller.

1098 The advantage of the x-ray dataset over the cosmics dataset is that absolute local offsets  
1099 are measurable thanks to the reference frame provided by the alignment platforms. This is  
1100 required to measure the position of strips in the ATLAS coordinate system and to satisfy the  
1101 NSWs' precision tracking goals. The x-ray local offsets are being used to build an alignment  
1102 model of strips in each quadruplet. It is compelling to imagine using the cosmics relative  
1103 local offsets to improve the model considering their precision and ability to capture effects  
1104 across the entire area of the quadruplet.

# 1105 Chapter 8

## 1106 Outlook and summary

### 1107 Outlook

1108 The results presented in this thesis pave the way to the further application of the rich cosmic  
1109 muon data set to alignment work. First, a systematic study of cosmic ray and x-ray relative  
1110 local strip position offsets should be performed for all quadruplets built for the NSWs. The  
1111 correlation plots such as those presented in figure 7.2 and 7.3 can reveal unexpected results  
1112 which could indicate an issue with either cosmic ray or x-ray data collection to be investigated  
1113 further. Then, the overall correlation between x-ray and cosmic datasets should be quantified  
1114 for all quadruplets instead of being quantified for each quadruplet individually.

1115 For now, the correlation of the individual quadruplets tested supports the use of the x-ray  
1116 data to build an alignment model. Work on the alignment model is ongoing [8]. Currently,  
1117 the algorithm compares the offsets of a local group of strips at each x-ray gun position as  
1118 measured by the x-ray and CMM methods in a fit to extract a global slope ( $m$ ) and offset  
1119 ( $b$ ) per layer,  $i$ , where the  $\chi^2$  is given by equation 8.1.

$$\chi^2 = \frac{[dy_{cmm,corr} - dy_{xray}]^2}{\delta dy_{xray}^2 + \delta dy_{cmm,corr}^2}, \quad (8.1)$$

1120

$$dy_{cmm,corr} = y_{cmm} + b_i + m_i x - y_{nom} \quad (8.2)$$

1121 Here,  $dy$  is a local strip position offset as calculated from the x-ray and corrected CMM data  
1122 and  $\delta dy$  refers to their respective uncertainties. The plan is that the alignment parameters  
1123 will be provided to the ATLAS experiment's offline software to reconstruct muon tracks  
1124 from the NSWs' sTGCs. The large uncertainty on the x-ray local offsets (120  $\mu\text{m}$ ) and

1125 the sparseness of the measurements means that including input from other characterization  
1126 datasets could reduce the uncertainty on the alignment model parameters.

1127 Relative local strip position offsets measured using cosmic ray data provide alignment in-  
1128 formation between the x-ray measurement points and can be calculated with a precision  
1129 relevant to alignment studies. Therefore provide additional and complementary information  
1130 that could further constrain the global rotation and translation parameter of the simple  
1131 misalignment model currently being used. Work on using the three datatsets at once in a  
1132 fit has begun.

## 1133 Summary

1134 The LHC [1] will be at the energy frontier of particle physics for at least the next decade,  
1135 making it a unique tool with which to study particle physics. With the HL-LHC [2], high  
1136 statistics on rare particle physics processes will enable more precise measurements of param-  
1137 eters of the Standard Model and increase the sensitivity to signatures of physics beyond the  
1138 Standard Model [3]. To capitalize on the increased luminosity, the muon small wheels of the  
1139 ATLAS experiment must be replaced to keep the triggering and tracking performance [5].

1140 Small-strip thin gap chambers are gas ionization chambers optimized for a high rate envi-  
1141 ronment [5]. Using the pad electrodes to define a region of interest makes it possible to get  
1142 track segments of  $\sim 1$  mrad angular resolution quickly, which will be used as input to check  
1143 if a collision originated from the interaction point and should be triggered on or not [5, 53].  
1144 Thanks to the careful design of the gas gaps and the small pitch of the strip readout elec-  
1145 trodes, sTGCs are also able to provide better than  $100\text{ }\mu\text{m}$  position resolution per detector  
1146 plane to fulfill precision offline tracking requirements [6].

1147 Ultimately, the positions of the sTGC strip electrodes need to be known in ATLAS to within  
1148  $\sim 100\text{ }\mu\text{m}$  so that they can deliver the required position resolution. The strategy is to build  
1149 an alignment model to estimate the position of each strip. Input to the alignment model  
1150 comes from the datasets used to characterize the quadruplets. The x-ray data [8] is the only  
1151 characterization dataset that directly links the position of the strips to the ATLAS coordinate  
1152 system. The alignment model could be built on x-ray data alone, but the sparseness of and  
1153 large uncertainty on the local offsets mean that the alignment model could benefit from more  
1154 input. The x-ray method is also a new technique that should be independently validated.

1155 Relative local offsets measured with the cosmics and x-ray datasets were compared and the  
1156 observed correlation confirmed the local offsets measured with the x-ray gun, validating the  
1157 x-ray method. Moreover, the cosmics relative local offsets are useful on their own. The 2D  
1158 visualizations of relative local offsets make it possible to quickly identify areas of misaligned

1159 strips and make hypotheses as to the physical origin of those misalignments. Also, the  
1160 cosmics residual means were shown to be robust and have uncertainties under  $100\text{ }\mu\text{m}$  for  
1161 all two-fixed-layer reference frames, which is small. Therefore, the cosmics relative local  
1162 offsets complement the x-ray data by providing a complete, robust picture of the relative  
1163 strip position offsets between layers. The next goal will be to use the cosmics relative local  
1164 offsets to improve the alignment model and better position the sTGC strips in ATLAS.

1165 Muons are important signatures of electroweak and Higgs sector events that physicists an-  
1166 ticipate studying with a high-statistics dataset [3, 5]. An effective alignment model of sTGC  
1167 strip positions will ensure that the NSWs can be used to accomplish the ATLAS collabora-  
1168 tion’s physics goals during the High Luminosity era of the LHC.

# <sup>1169</sup> References

- <sup>1170</sup> [1] L. Evans and P. Bryant. LHC Machine. *Journal of Instrumentation*, 3(S08001), August  
<sup>1171</sup> 2008.
- <sup>1172</sup> [2] G. Apollinari et al. High-Luminosity Large Hadron Collider (HL-LHC) Technical Design  
<sup>1173</sup> Report V. 0.1. Technical Report CERN-2017-007-M, CERN, Geneva, September 2017.
- <sup>1174</sup> [3] A. Dainese et al. The physics potential of HL-LHC. In *Input to the European Particle  
1175 Physics Strategy Update*, November 2018.
- <sup>1176</sup> [4] The ATLAS Collaboration. The ATLAS Experiment at the CERN Large Hadron Col-  
<sup>1177</sup> linder. *Journal of Instrumentation*, 3(08):S08003, August 2008.
- <sup>1178</sup> [5] T. Kawamoto et al. New Small Wheel Technical Design Report. Technical Report  
<sup>1179</sup> CERN-LHCC-2013-006, ATLAS-TDR-020, CERN, Geneva, June 2013.
- <sup>1180</sup> [6] A. Abusleme et al. Performance of a Full-Size Small-Strip Thin Gap Chamber Prototype  
<sup>1181</sup> for the ATLAS New Small Wheel Muon Upgrade. *Nuclear Instruments and Methods in  
1182 Physics Research Section A: Accelerators, Spectrometers, Detectors and Associated  
1183 Equipment*, 817:85–92, May 2016. arXiv: 1509.06329.
- <sup>1184</sup> [7] E.M. Carlson. *Results of the 2018 ATLAS sTGC test beam and internal strip alignment  
1185 of sTGC detectors*. M.Sc. thesis, University of Victoria, Victoria, Canada, 2019.
- <sup>1186</sup> [8] B. Lefebvre. Precision survey of the readout strips of small-strip Thin Gap Chambers  
<sup>1187</sup> using X-rays for the muon spectrometer upgrade of the ATLAS experiment. *Journal of  
1188 Instrumentation*, 15(07):C07013–C07013, July 2020.
- <sup>1189</sup> [9] D.J. Griffiths. *Introduction to elementary particles*. Physics textbook. Wiley-VCH,  
<sup>1190</sup> Weinheim, Germany, 2., rev. ed., 5. reprint edition, 2011.
- <sup>1191</sup> [10] M.E. Peskin and D.V. Schroeder. *An introduction to quantum field theory*. Addison-  
<sup>1192</sup> Wesley Pub. Co, Reading, Massachusetts, 1995.

- 1193 [11] P.A. Zyla et al. Review of Particle Physics. *PTEP*, 2020(8):083C01, 2020.
- 1194 [12] M. Kobayashi and T. Maskawa. CP-violation in the renormalizable theory of weak  
1195 interaction. *Progress of theoretical physics*, 49(2):652–657, February 1973.
- 1196 [13] M.L. Perl et al. Evidence for Anomalous Lepton Production in  $\{e\}^{\{+}\backslash ensuremath{-}\} \{e\}^{\backslash ensuremath{-}\}}$ Annihilation. *Physical Review Letters*, 35(22):1489–1492, De-  
1197 cember 1975. Publisher: American Physical Society.$
- 1198 [14] F. Englert and R. Brout. Broken Symmetry and the Mass of Gauge Vector Mesons.  
1199 *Physical Review Letters*, 13(9):321–323, August 1964. Publisher: American Physical  
1200 Society.
- 1201 [15] P.W. Higgs. Broken symmetries, massless particles and gauge fields. *Physics Letters*,  
1202 12(2):132–133, September 1964.
- 1203 [16] D. Galbraith and C. Burgard. UX: Standard Model of the Stan-  
1204 dard Model, November 2013. [http://davidgalbraith.org/portfolio/  
1205 ux-standard-model-of-the-standard-model/](http://davidgalbraith.org/portfolio/ux-standard-model-of-the-standard-model/) last accessed on 2021-09-30.
- 1206 [17] C.A. Bertulani. *Nuclear physics in a nutshell*. In a nutshell. Princeton University Press,  
1207 Princeton, N.J, 2007. OCLC: ocm85690422.
- 1208 [18] B.W. Carroll and D.A. Ostlie. *An introduction to modern astrophysics*. Pearson  
1209 Addison-Wesley, San Francisco, 2nd ed edition, 2007. OCLC: ocm69020924.
- 1210 [19] M. Boezio and E. Mocchiutti. Chemical composition of galactic cosmic rays with space  
1211 experiments. *Astroparticle Physics*, 39-40:95–108, December 2012.
- 1212 [20] The SNO Collaboration. Combined analysis of all three phases of solar neutrino data  
1213 from the sudbury neutrino observatory. *Phys. Rev. C*, 88:025501, August 2013.
- 1214 [21] B. Pontecorvo. Neutrino Experiments and the Problem of Conservation of Leptonic  
1215 Charge. *Soviet Physics—JETP*, 53:1717–1725, 1967.
- 1216 [22] S.M. Bilenky and S.T. Petcov. Massive neutrinos and neutrino oscillations. *Reviews of  
1217 Modern Physics*, 59(3):671–754, July 1987.
- 1218 [23] B. Young. A survey of dark matter and related topics in cosmology. *Frontiers of Physics*,  
1219 12(2):121201, April 2017.
- 1220 [24] C. Muñoz. Dark matter detection in the light of recent experimental results. *International  
1221 Journal of Modern Physics A*, 19(19):3093–3169, July 2004.

- 1223 [25] G. Arnison et al. Experimental observation of isolated large transverse energy elec-  
1224 trons with associated missing energy at s=540 GeV. *Physics Letters B*, 122(1):103–116,  
1225 February 1983.
- 1226 [26] M. Banner et al. Observation of single isolated electrons of high transverse momentum  
1227 in events with missing transverse energy at the CERN pp collider. *Physics Letters B*,  
1228 122(5):476–485, March 1983.
- 1229 [27] G. Arnison et al. Experimental observation of lepton pairs of invariant mass around 95  
1230 GeV/c<sup>2</sup> at the CERN SPS collider. *Physics Letters B*, 126(5):398–410, July 1983.
- 1231 [28] P. Bagnaia et al. Evidence for Z → e<sup>+</sup>e<sup>-</sup> at the CERN pp collider. *Physics Letters B*,  
1232 129(1):130–140, 1983.
- 1233 [29] The CDF Collaboration. Observation of Top Quark Production in  $\bar{p}p$  Collisions with  
1234 the Collider Detector at Fermilab. *Physical Review Letters*, 74(14):2626–2631, April  
1235 1995. Publisher: American Physical Society.
- 1236 [30] The D0 Collaboration. Observation of the Top Quark. *Physical Review Letters*,  
1237 74(14):2632–2637, April 1995. Publisher: American Physical Society.
- 1238 [31] The ATLAS Collaboration. Observation of a new particle in the search for the Standard  
1239 Model Higgs boson with the ATLAS detector at the LHC. *Physics Letters B*, 716(1):1–  
1240 29, September 2012. arXiv: 1207.7214.
- 1241 [32] The CMS Collaboration. Observation of a new boson at a mass of 125 GeV with the  
1242 CMS experiment at the LHC. *Physics Letters B*, 716(1):30–61, September 2012. arXiv:  
1243 1207.7235.
- 1244 [33] Standard Model Summary Plots June 2021, June 2021. <https://atlas.web.cern.ch/Atlas/GROUPS/PHYSICS/PUBNOTES/ATL-PHYS-PUB-2021-032/> last accessed on 2021-  
1245 09-30.
- 1247 [34] O.S. Brüning et al. LHC Design Report. Design Report CERN-2004-003-V-1, CERN,  
1248 CERN, Geneva, Switzerland, 2004. ISBN: 9789290832249.
- 1249 [35] ATLAS luminosity public results run-1, March 2011. <https://twiki.cern.ch/twiki/bin/view/AtlasPublic/LuminosityPublicResults> last accessed on 2021-09-20.
- 1251 [36] ATLAS luminosity public results run-2, July 2015. <https://twiki.cern.ch/twiki/bin/view/AtlasPublic/LuminosityPublicResultsRun2> last accessed on 2021-09-20.

- 1253 [37] The European Strategy for Particle Physics. Technical Report CERN/2685, CERN,  
1254 2006. Adopted by the CERN council at a special session at ministerial level in Lisbon  
1255 in 2006.
- 1256 [38] HiLumi HL-LHC Project. LHC/HL-LHC plan (last update january 2021). <https://hilumilhc.web.cern.ch/content/hl-lhc-project>, last accessed on 2021-09-09.
- 1258 [39] M. Cepeda et al. Report from Working Group 2: Higgs Physics at the HL-LHC and  
1259 HE-LHC. In A. Dainese et al., editors, *Report on the Physics at the HL-LHC, and*  
1260 *Perspectives for the HE-LHC*, number CERN-LPCC-2018-04, pages 221–584. 364 p,  
1261 CERN, Geneva, Switzerland, Jun 2018. CERN.
- 1262 [40] ATLAS inner detector : Technical Design Report, 1. Technical Report CERN-LHCC-  
1263 97-016, CERN, April 1997. ISBN: 9789290831020 Publication Title: CERN Document  
1264 Server.
- 1265 [41] S. Haywood, L. Rossi, R. Nickerson, and A. Romanouk. ATLAS inner detector :  
1266 Technical Design Report, 2. Technical Report CERN-LHCC-97-017, CERN, April 1997.  
1267 ISBN: 9789290831037 Publication Title: CERN Document Server.
- 1268 [42] C. Grupen, B.A. Shwartz, and H. Spieler. *Particle detectors*. Cambridge University  
1269 Press, Cambridge, UK; New York, 2008. OCLC: 1105536566.
- 1270 [43] ATLAS liquid-argon calorimeter : Technical Design Report. Technical Report CERN-  
1271 LHCC-96-041, CERN, 1996. ISBN: 9789290830900 Publication Title: CERN Document  
1272 Server.
- 1273 [44] ATLAS tile calorimeter : Technical Design Report. Technical Report CERN-LHCC-96-  
1274 042, CERN, 1996. ISBN: 9789290830917 Publication Title: CERN Document Server.
- 1275 [45] The ATLAS Collaboration. ATLAS Muon Spectrometer: Technical Design Report.  
1276 Technical Report CERN-LHCC-97-022, CERN, Geneva, 1997.
- 1277 [46] ATLAS magnet system : Technical Design Report, 1. Technical Report CERN-LHCC-  
1278 97-018, CERN, April 1997. ISBN: 9789290831044 Publication Title: CERN Document  
1279 Server.
- 1280 [47] The ATLAS Collaboration. Performance of the ATLAS muon trigger in pp collisions  
1281 at  $\sqrt{s} = 8$  TeV. *The European Physical Journal C*, 75(3):120, March 2015. arXiv:  
1282 1408.3179.

- 1283 [48] S. Aefsky et al. The Optical Alignment System of the ATLAS Muon Spectrometer End-  
1284 caps. *Journal of Instrumentation*, 3(11):P11005–P11005, November 2008. Publisher:  
1285 IOP Publishing.
- 1286 [49] ATLAS level-1 trigger : Technical Design Report. Technical Report CERN-LHCC-98-  
1287 014, CERN, August 1998. ISBN: 9789290831280 Publication Title: CERN Document  
1288 Server.
- 1289 [50] A. Ruiz Martínez. The run-2 ATLAS trigger system. *Journal of Physics: Conference  
1290 Series*, 762:012003, October 2016.
- 1291 [51] Technical Design Report for the Phase-II Upgrade of the ATLAS TDAQ System. Tech-  
1292 nical Report CERN-LHCC-2017-020, ATLAS-TDR-029, CERN, Geneva, September  
1293 2017.
- 1294 [52] P. Jenni, M. Nessi, M. Nordberg, and K. Smith. ATLAS high-level trigger, data-  
1295 acquisition and controls : Technical Design Report. Technical Report CERN-LHCC-  
1296 2003-022, CERN, July 2003.
- 1297 [53] E. Perez Codina. Small-strip Thin Gap Chambers for the muon spectrometer upgrade of  
1298 the ATLAS experiment. *Nuclear Instruments and Methods in Physics Research Section  
1299 A: Accelerators, Spectrometers, Detectors and Associated Equipment*, 824:559–561, July  
1300 2016.
- 1301 [54] J. Townsend. *Electricity in gases*. Clarendon Press, Oxford, 1915.
- 1302 [55] S. Majewski, G. Charpak, A. Breskin, and G. Mikenberg. A thin multiwire chamber  
1303 operating in the high multiplication mode. *Nuclear Instruments and Methods*, 217:265–  
1304 271, 1983.
- 1305 [56] E. Gatti, A. Longoni, H. Okuno, and P. Semenza. Optimum geometry for strip cathodes  
1306 or grids in MWPC for avalanche localization along the anode wires. *Nuclear Instruments  
1307 and Methods*, 163(1):83–92, July 1979.
- 1308 [57] G. Battistoni et al. Resistive cathode transparency. *Nuclear Instruments and Methods  
1309 in Physics Research*, 202(3):459–464, November 1982.
- 1310 [58] B. Lefebvre. *Characterization studies of small-strip Thin Gap Chambers for the ATLAS  
1311 Upgrade*. PhD thesis, McGill University, Montreal, Canada, 2018.
- 1312 [59] P.K.F. Grieder. *Cosmic rays at Earth: researcher’s reference manual and data book*.  
1313 Elsevier Science Ltd, Amsterdam, 1st ed edition, 2001.

- 1314 [60] R. Keyes et al. Development and characterization of a gas system and its associated  
 1315 slow-control system for an ATLAS small-strip thin gap chamber testing facility. *Journal*  
 1316 *of Instrumentation*, 12(04):P04027–P04027, April 2017.
- 1317 [61] Georgios Iakovidis. VMM3, an ASIC for Micropattern Detectors. Technical Report  
 1318 ATL-MUON-PROC-2018-003, CERN, Geneva, March 2018.
- 1319 [62] B. Chen. *Calibration Studies of the Front-End Electronics for the ATLAS New Small*  
 1320 *Wheel Project*. M.Sc. thesis, McGill University, Montreal, Canada, 2019.
- 1321 [63] R. Brun and F. Rademakers. ROOT: An object oriented data analysis framework. *Nu-*  
 1322 *clear Instruments and Methods in Physics Research Section A: Accelerators, Spectrome-*  
 1323 *ters, Detectors and Associated Equipment*, 389:81–86, 1997. See also ”ROOT” [software],  
 1324 Release 6.18/02, 23/08/2019, (<https://zenodo.org/record/3895860#.YVJW6n0pCHs>).
- 1325 [64] F. Sauli. Principles of operation of multiwire proportional and drift chambers. Number 81 in CERN Academic Training Lectures, CERN, Geneva, Switzerland, September  
 1326 1975 – June 1976. CERN.
- 1327 [65] M. Hatlo et al. Developments of mathematical software libraries for the LHC experi-  
 1328 ments. *IEEE Transactions on Nuclear Science*, 52:2818–2822, 2005.
- 1329 [66] H. Guo. A Simple Algorithm for Fitting a Gaussian Function [DSP Tips and Tricks].  
 1330 *IEEE Signal Processing Magazine*, 28(5):134–137, September 2011.
- 1331 [67] I. Endo et al. Systematic shifts of evaluated charge centroid for the cathode read-out  
 1332 multiwire proportional chamber. *Nuclear Instruments and Methods in Physics Research*,  
 1333 188(1):51–58, September 1981.
- 1334 [68] Minature x-ray source mini-x. Product of Amptek Inc. <https://www.amptek.com/-/media/ametekamptek/documents/resources/specs/mini-x-specifications.pdf?la=en&revision=512f7eb3-01b3-47fd-864f-5525c850fc6e&hash=B8B03C0592486E2D91C566C4326F15F5>, last accessed on 2021-10-15.
- 1335 [69] B. Stelzer. The New Small Wheel Upgrade Project of the ATLAS Experiment. *Nuclear*  
 1336 *and Particle Physics Proceedings*, 273-275:1160–1165, April 2016.
- 1337 [70] X. Zhao et al. Cosmic test of sTGC detector prototype made in China for ATLAS  
 1338 experiment upgrade. *Nuclear Instruments and Methods in Physics Research Section A:*  
 1339 *Accelerators, Spectrometers, Detectors and Associated Equipment*, 927:257–261, May  
 1340 2019.

<sup>1345</sup> APPENDICES

<sub>1346</sub> **Appendix A**

<sub>1347</sub> **Uncertainty in cluster positions**

<sub>1348</sub> The clusters were fit with Guo’s method [66] and Minuit2 for ROOT [65]. The difference in  
<sub>1349</sub> cluster means between the two algorithms is shown in figure A.1.

<sub>1350</sub> The RMS of the distribution in figure A.1 is 57  $\mu\text{m}$ , which is much larger than the statistical  
<sub>1351</sub> uncertainty in the mean for the Minuit2 algorithm, which peaks around 7  $\mu\text{m}$ . An RMS of  
<sub>1352</sub> 60  $\mu\text{m}$  is common for data taken with most quadruplets at 3.1 kV. Therefore, the uncer-  
<sub>1353</sub> tainty in the reconstructed cluster  $y$ -coordinate is assigned 60  $\mu\text{m}$  due to variations in the  
<sub>1354</sub> reconstruction with different Gaussian fit algorithms.

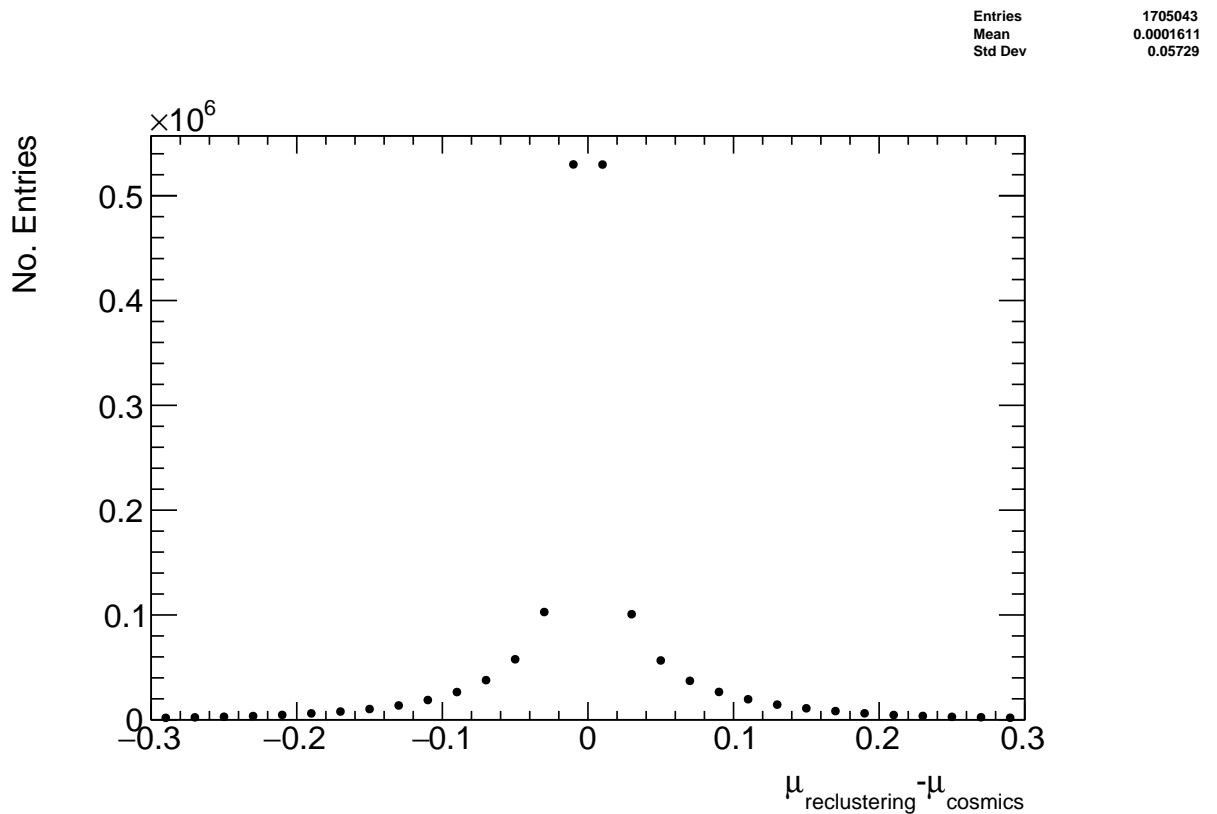


Figure A.1: The difference between cluster means calculated with Guo's method [66] in `tgc_analysis/CosmicsAnalysis` and Minuit2 for ROOT [65] in `strip_position_analysis/ReClustering` for data collected with QL2.P.8 at 3.1 kV.

1355 **Appendix B**

1356 **Study of cosmics for alignment  
1357 analysis statistical uncertainty**

1358 Typically, one million triggers (cosmic muon events, noise, photons and  $\delta$ -rays) were collected  
1359 for each Canadian quadruplet at McGill University, resulting in roughly half the number of  
1360 viable tracks after cuts. For QS3.P.18, 3.5 million triggers were collected. To gauge the  
1361 sensitivity of the analysis to the available statistics, partitions of this data with each with  
1362 a different number of triggers were analyzed separately. Ultimately, the quantity of interest  
1363 was the Gaussian mean of the residual distribution in regions of interest, so the peak in the  
1364 distribution of the statistical uncertainty in the residual means for each area of interest for  
1365 a specific tracking combination was used to gauge the quality of the analysis. How the peak  
1366 in the residual mean uncertainty distribution changes with the number of triggers is shown  
1367 in figure for tracks on layer 1 built from layers 3 and 4 [B.1](#).

1368 The uncertainty is already around 20  $\mu\text{m}$  at 1 million triggers, suitable for distinguishing  
1369 differences in offsets of order 50  $\mu\text{m}$  as required. Although increased statistics could decrease  
1370 the statistical uncertainty, it is not required for the goals of this analysis. Moreoever, the  
1371 systematic uncertainty on the mean cosmics residuals is around 50  $\mu\text{m}$  so the statistical  
1372 uncertainty of 20  $\mu\text{m}$  is nearly negligible.

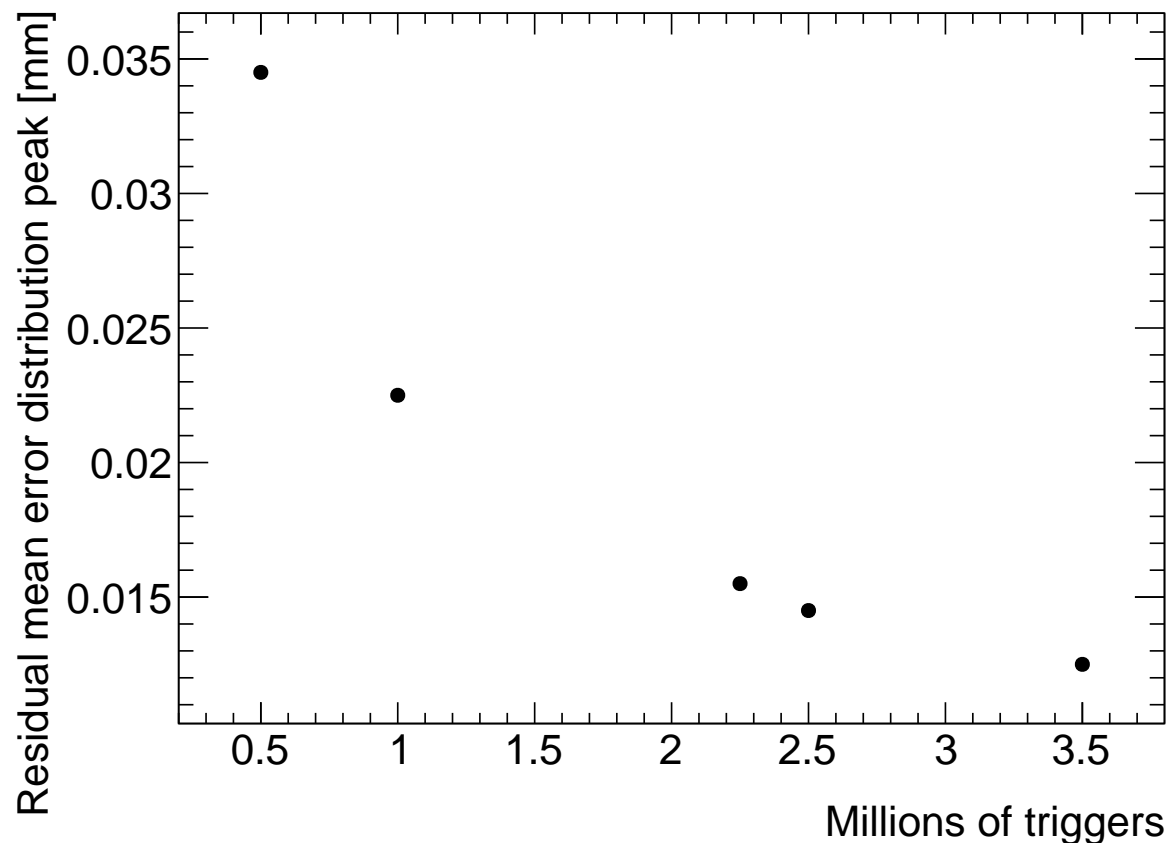


Figure B.1: How the peak of the distributions of uncertainties in the residual means in regions of interest for tracks on layer 1 built from layers 3 and 4 changed with the number of triggers used in the analysis. The distribution falls off as  $\frac{1}{\sqrt{N}}$  as expected.

# 1373 Appendix C

## 1374 Study of systematic uncertainties 1375 when using cosmics data for 1376 alignment studies

### 1377 C.1 Residual distribution fit function

1378 The distribution of residuals should be modeled by a double Gaussian fit[58]:

$$G(r) = A_s \exp\left[\frac{-(r - \mu)^2}{2\sigma_s^2}\right] + A_b \exp\left[\frac{-(r - \mu)^2}{2\sigma_b^2}\right] \quad (\text{C.1})$$

1379 where  $r$  is the residual,  $A$  is the Gaussian amplitude,  $\mu$  is the Gaussian mean,  $\sigma$  is the  
1380 Gaussian sigma, and the subscripts  $s$  and  $b$  stand for signal and background respectively.  
1381 One Gaussian captures the real (signal) tracks and the other captures the tracks built from  
1382 noise (background). The Gaussian with the smaller width is identified as the signal.

1383 A single Gaussian fit failed less often than a double Gaussian fit. The Gaussian fits were  
1384 performed by initially estimating the amplitude to be 100 tracks, the Gaussian mean to be  
1385 the histogram mean, and Gaussian  $\sigma$  to be the RMS. The fit range was restricted to  $\pm 1$   
1386 root-mean-square (RMS) from the histogram mean. The modification helped the Gaussian  
1387 fit capture the signal peak. An example residual distribution is shown in figure C.1.

1388 For all residual distributions in 100 mm by 100 mm bins on layer 4 built from clusters on  
1389 layers 1 and 2, the difference in Gaussian and double Gaussian means and  $\sigma$ 's is shown in  
1390 figure C.2a. The mean of the distribution is centered around zero (within the RMS of the

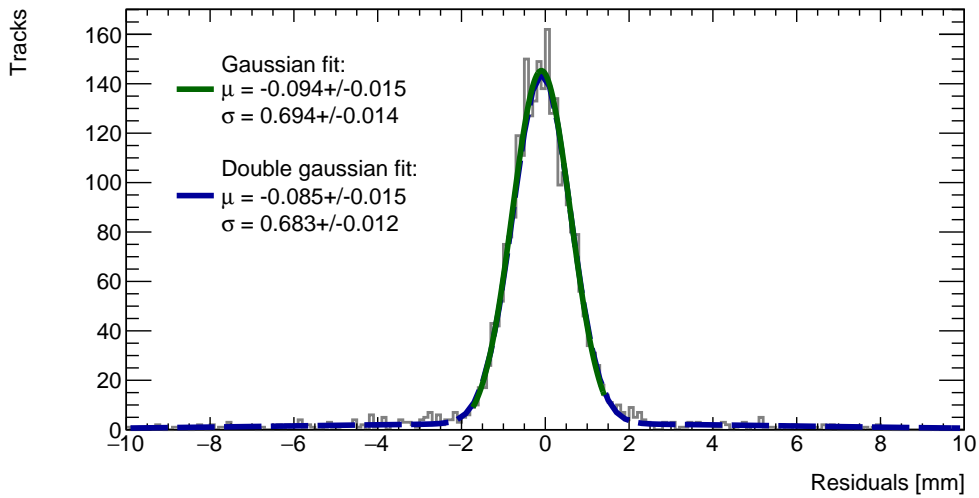
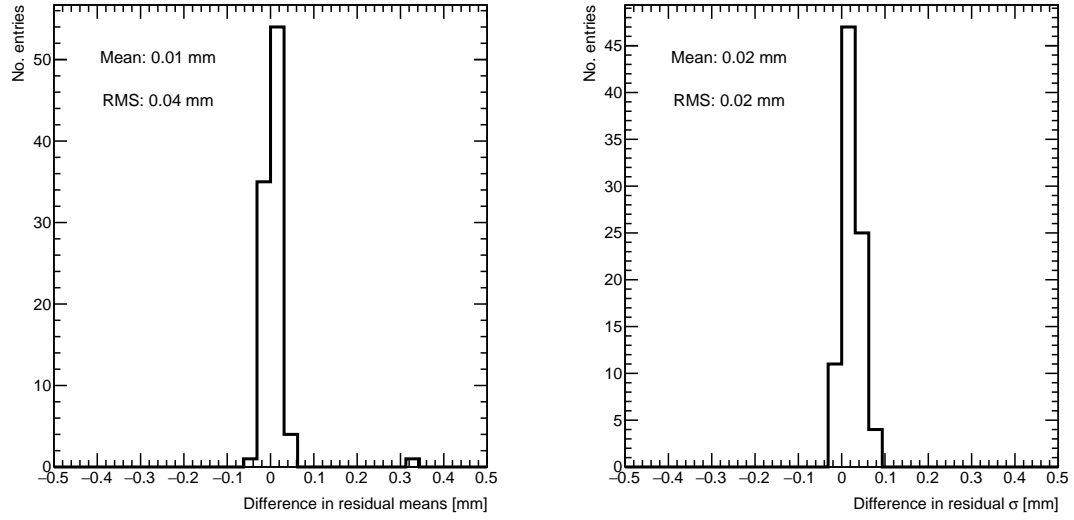


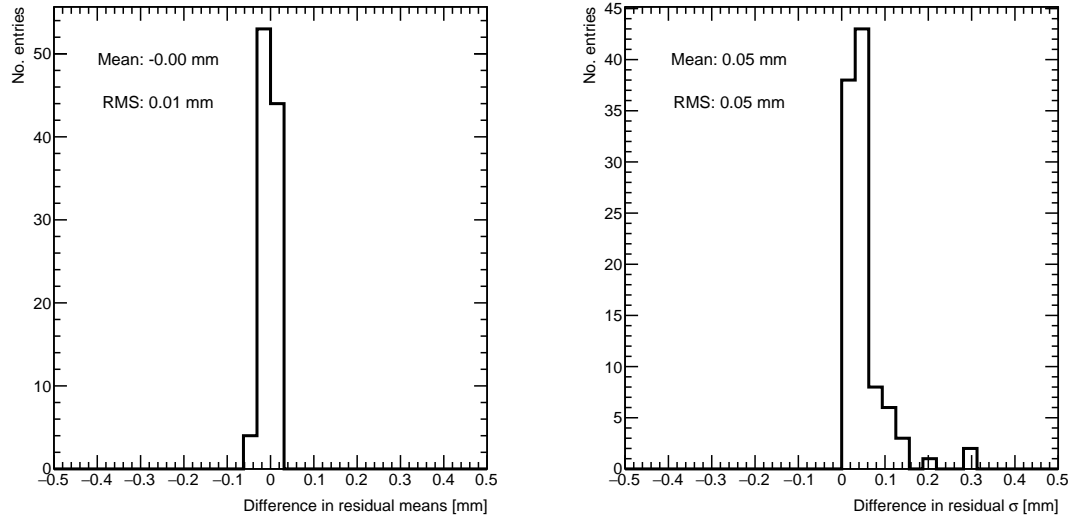
Figure C.1: Residual distribution for track residuals on layer 4 built from clusters on layers 1 and 2 for  $x \in [-3.00, 97.00]$  mm,  $y \in [394.60, 494.60]$  mm, fit with a double Gaussian and a single Gaussian in a range of  $\pm 1$  RMS from the histogram mean.

1391 distribution) so the choice of fit algorithm imbues no measurable bias. The order of the  
1392 RMS is such that the difference in residual means at 40  $\mu\text{m}$  is just significant, so it should  
1393 be accounted for as a systematic uncertainty on the Gaussian residual means. The 40  $\mu\text{m}$   
1394 RMS is for the tracking combination with the worst extrapolation lever arm and the widest  
1395 distribution of mean differences; the interpolation combinations have narrower distributions,  
1396 as shown in figure C.2b. The RMS of the distribution for residual means on layer 2 obtained  
1397 using reference layers 1 and 3 is only 10  $\mu\text{m}$ , which is almost negligible.

1398 The Gaussian  $\sigma$  should be larger than the double Gaussian  $\sigma$  because the Gaussian distri-  
1399 bution includes the effect of the noise tracks that can yield large residuals, while the double  
1400 Gaussian models signal and background residuals separately. For this analysis, only the  
1401 residual mean was important, so the systematic overestimate of the signal  $\sigma$  in the Gaussian  
1402 fit shown in the right-side plots of figure C.2 was allowed.



(a) Difference in residual distribution means (left) and  $\sigma$ 's (right) extracted with a Gaussian and double Gaussian fit, for all residual distributions in 100 mm by 100 mm bins on layer 4 built from clusters on layers 1 and 2 for sample quadruplet QL2.P.8.



(b) Difference in residual distribution means (left) and  $\sigma$ 's (right) for a Gaussian and double Gaussian fit, for all residual distributions in 100 mm by 100 mm bins on layer 2 built from clusters on layers 1 and 3 for sample quadruplet QL2.P.8.

Figure C.2

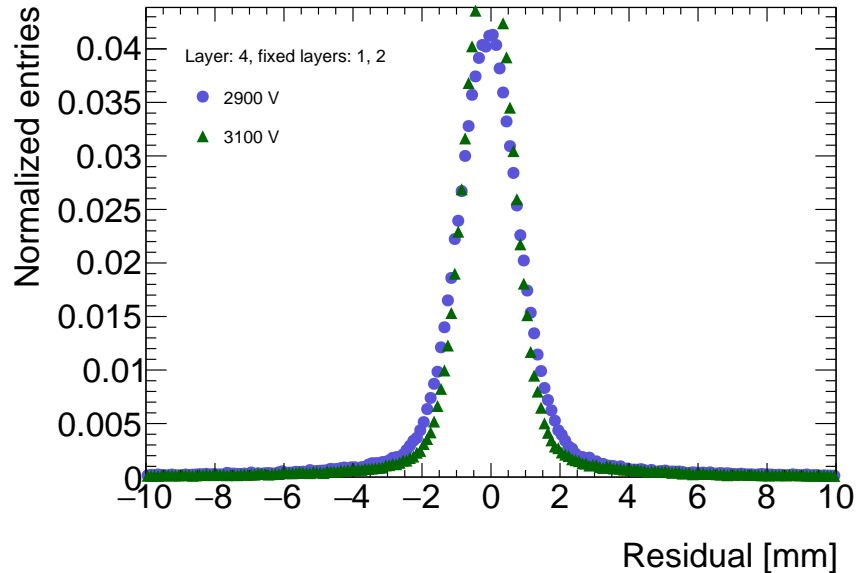


Figure C.3: Residual distribution for tracks on layer 4 built from clusters on layers 1 and 2 for sample quadruplet QL2.P.8 for data collected at 2.9 kV and 3.1 kV.

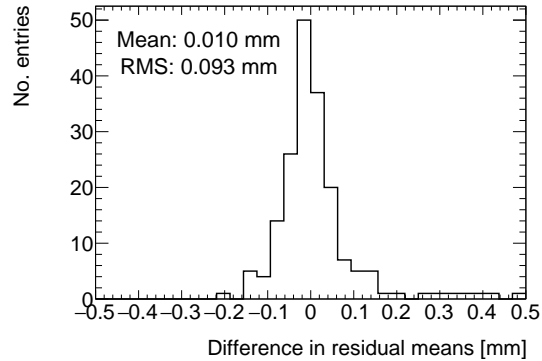
<sup>1403</sup> Ultimately, a Gaussian fit was chosen for the track residual distributions because it was more  
<sup>1404</sup> robust and did not affect the fitted mean values too strongly.

## <sup>1405</sup> C.2 Cosmic muon data collection voltage

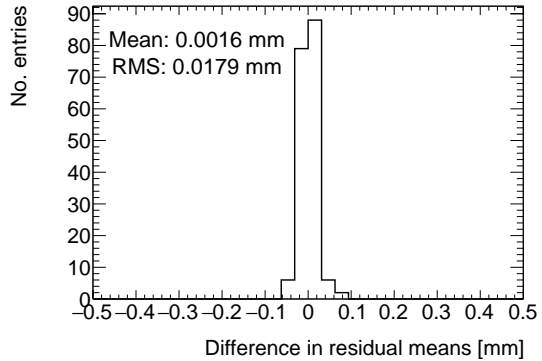
<sup>1406</sup> Cosmic muon data was collected at 2.9 kV and 3.1 kV because although 2.9 kV is closer to  
<sup>1407</sup> the operating conditions the chambers will be subject to in ATLAS, the extra gain provided  
<sup>1408</sup> by operating at 3.1 kV increased the signal to noise ratio for pad signals. Also, the tracking  
<sup>1409</sup> efficiency was higher with data collected at 3.1 kV. As such, cosmic muon data collected at  
<sup>1410</sup> 3.1 kV was used in the analysis presented in the body of the thesis.

<sup>1411</sup> The difference in gain affects the relative population of clusters of different sizes, which in  
<sup>1412</sup> turn affects the uncertainty in the mean cluster positions on each layer, the uncertainty in  
<sup>1413</sup> the track positions and the residual distributions. The residual distributions for 3.1 kV data  
<sup>1414</sup> are narrower, as shown in figure C.3.

<sup>1415</sup> Neither dataset is better for calculating the mean of residuals in a given area, so a systematic  
<sup>1416</sup> uncertainty can be assigned based on the difference in residual means calculated for 2.9 kV  
<sup>1417</sup> and 3.1 kV data per tracking combination. For each tracking combination, the difference



(a) Difference in residual means when measured with residuals on layer 4 built from clusters on layers 1 and 2.



(b) Difference in residual means when measured with residuals on layer 2 built from clusters on layers 1 and 3.

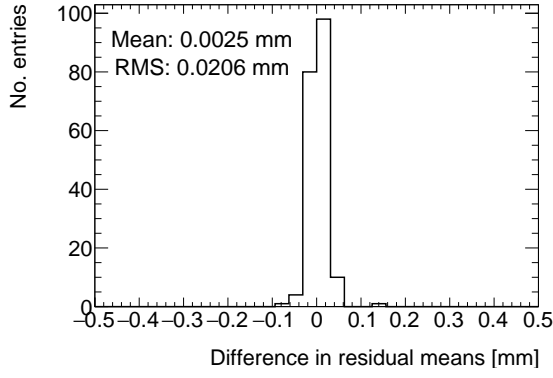
Figure C.4: Difference in residual means for data collected with sample quadruplet QL2.P.8 at 2.9 kV and 3.1 kV respectively in 100 mm by 100 mm bins.

in the fitted track residual means in 100 mm by 100 mm areas for 2.9 kV and 3.1 kV data are put in a distribution for a sample quadruplet, as shown in figure C.4. The means of the distributions for both tracking combinations are near zero, so as expected the collection voltage introduces no bias. Tracks built from clusters on layers 1 and 2 and extrapolated to layer 4 have the worst lever arm and hence the largest root-mean-square (RMS) of 100  $\mu\text{m}$ . The width of the distributions for geometrically favourable tracking combinations are much narrower. The narrowest width of the residual mean difference distribution is for tracks on layer 2 built from clusters on layers 1 and 3 (see figure C.4b), with a value of 20  $\mu\text{m}$ .

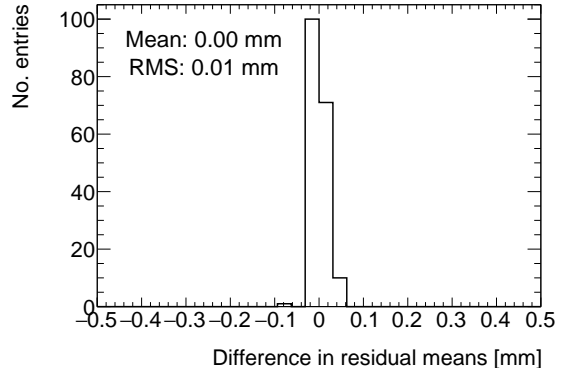
### C.3 Cluster fit algorithm

To ensure that changing the cluster fitting algorithm like in appendix A would not change the calculated mean of residuals in each region of interest significantly, the residual means were compared in both cases. The distribution of the difference in residual means is plotted in figure C.5 for the tracking combinations with the worst and most favourable extrapolation lever arms.

The mean of the distributions are centered around zero, so the choice of cluster fit algorithm did not introduce any bias. Differences on the order of 50  $\mu\text{m}$  are important, so the root-mean-squares (RMS's) of the distributions show that the clustering algorithm had a small but notable effect between 10-20  $\mu\text{m}$  from the most to least geometrically favourable tracking



(a) Difference in residual means when measured with residuals on layer 4 built from clusters on layers 1 and 2.



(b) Difference in residual means when measured with residuals on layer 2 built from clusters on layers 1 and 3.

Figure C.5: Difference in residual means when the cluster fit algorithm is `Minuit2` [65] versus Guo's method [66] for two different tracking combinations for sample quadruplet, QL2.P.8.

1436 combinations. Therefore, the RMS for each tracking combination will be used to add a  
 1437 systematic uncertainty on the residual means accounting for the effect that different cluster  
 1438 fit algorithms have on the residual means.

## 1439 C.4 Differential non-linearity

### 1440 Definition

1441 In this context, differential non-linearity (DNL) is when the reconstructed cluster mean is  
 1442 biased by the fit of the discretely sampled peak signal amplitude distribution over the strips.  
 1443 The bias depends on the relative position of the avalanche with respect to the center of the  
 1444 closest strip. For a summary of DNL, refer to page 40 of [58], an early paper studying its  
 1445 effects [67], and for an example application, refer to [6].

### 1446 Application and effect of DNL

1447 The cluster mean was corrected for DNL using the equation:

$$y' = y + a \sin(2\pi y_{rel}) \quad (\text{C.2})$$

1448 where  $y$  is the cluster mean,  $y_{rel}$  is the relative position of the cluster mean with respect  
 1449 to the strip's center,  $a$  is the amplitude of the correction, and  $y'$  is the corrected cluster

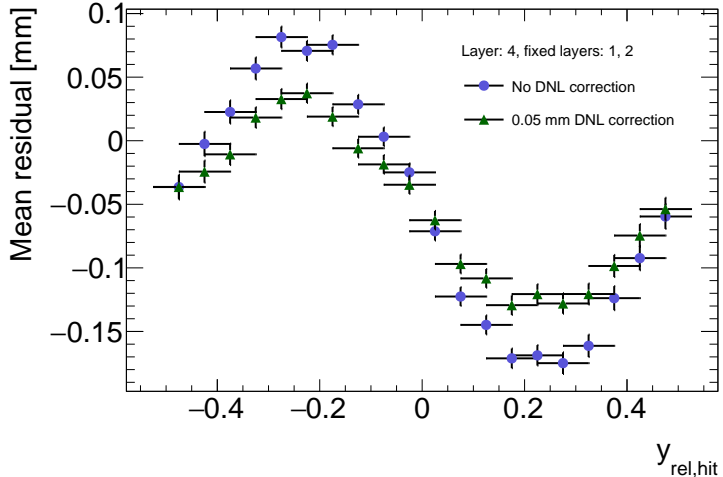


Figure C.6: Effect applying a  $50\text{ }\mu\text{m}$  DNL correction to the profile of the residuals sorted by  $y_{rel}$  for residuals built from clusters on layers 1 and 2 and extrapolated to layer 4 of quadruplet, QL2.P.8.

mean. The amplitude can be derived by comparing the reconstructed hit position to the expected hit position, as done in [6]. With cosmic muons, there is no reference hit position to compare to, so track residuals were used as a proxy [58]. The hallmark of the DNL effect is the periodic pattern in the residual versus  $y_{rel}$  profile, and the effect of correcting the cluster means using an amplitude of  $50\text{ }\mu\text{m}$  is shown in figure C.6. An amplitude of  $50\text{ }\mu\text{m}$  is based on Dr. Lefebvre's [58] estimate of the DNL amplitudes by layer, quadruplet and cluster size using cosmic muon tracks [58]. Little variation is seen in the amplitude parameters with respect to the quadruplet tested, the layer and the cluster size so a universal correction is used.

Although the correction is not large enough in this case, the figure shows that the correction does reduce the DNL effect. Slightly better performance is seen in the interpolation tracking combinations where the quality of the residuals is better. DNL corrections for cosmic muon data are difficult because the DNL effect is obscured by the effect of misalignments between strip layers and noise. Misalignments cause the center of the sinusoidal pattern in figure C.6 to be shifted off of zero, since the mean of residuals is shifted.

Figure C.7 shows the distribution of the difference in residual means calculated in  $100\text{ mm}$  by  $100\text{ mm}$  areas for mean track residuals on layer 4 obtained using layers 1 and 2 as reference. The mean of the distribution is zero within the root-mean-square so the DNL correction does not bias the residual means. It is apparent that the effect of the DNL correction on

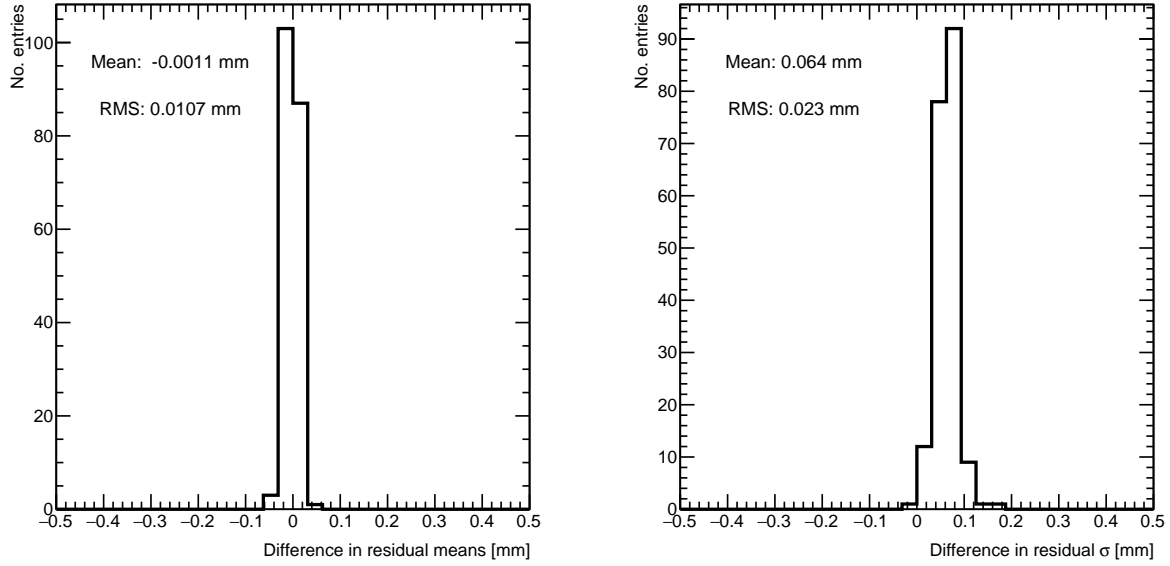


Figure C.7: Difference in residual distribution means and  $\sigma$ 's with and without DNL correction for residuals on layer 4 obtained using reference layers 1 and 2 for sample quadruplet, QL2.P.8.

the residual means is on the order of micrometers given the RMS of  $10 \mu\text{m}$  in the worst extrapolation case. Although the  $\sigma$ 's of the residual distributions shrink with the DNL correction, the mean is the parameter of interest so the bias in the fitted  $\sigma$ 's was ignored. Therefore, in this analysis DNL is not corrected for.

<sub>1473</sub> Appendix D

<sub>1474</sub> Printable plots

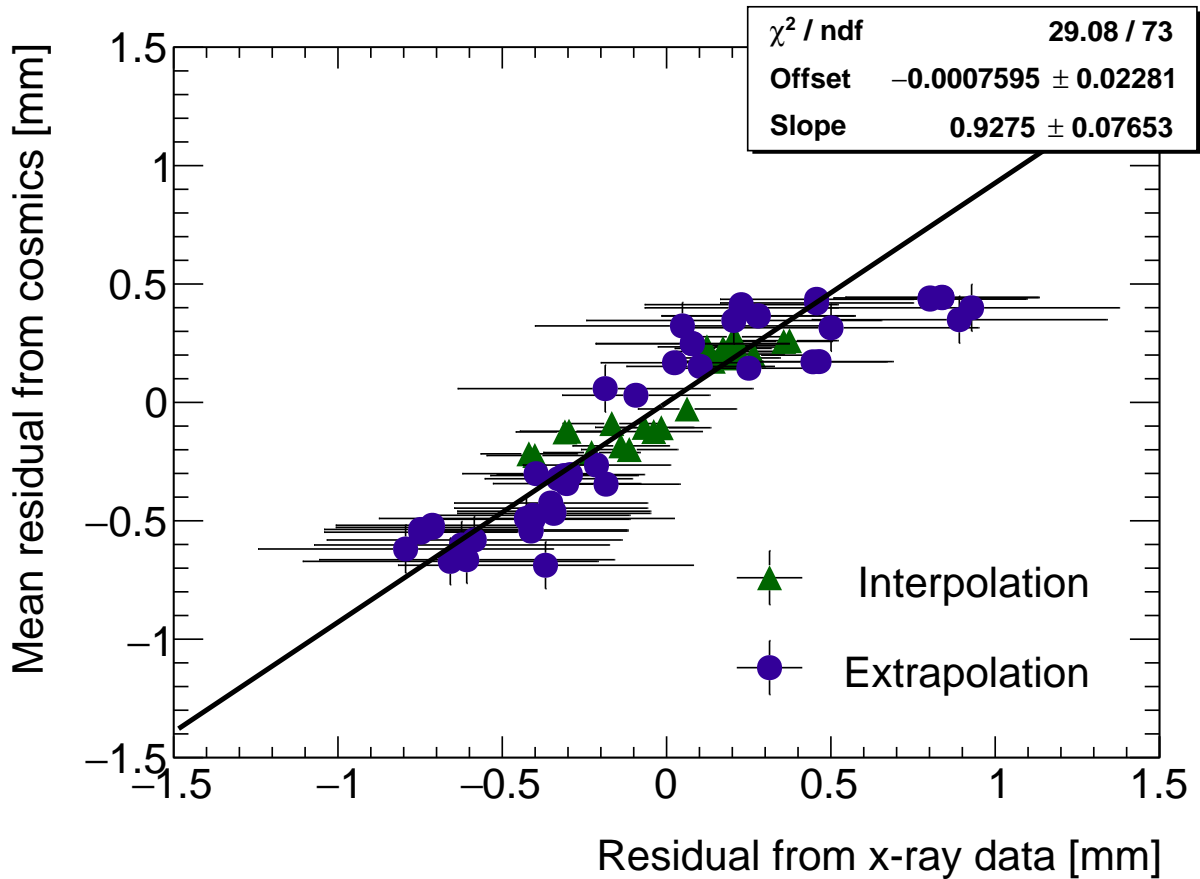


Figure D.1: Correlation plot between x-ray and cosmics residuals for all tracking combinations for QL2.P.11. Each rectangle is centered on an x-ray and mean cosmics residual pair. The width of the rectangles in  $x$  and  $y$  are the uncertainty in the x-ray and mean cosmics residual respectively. This is a printable version of figure 7.2 in section 7.1.

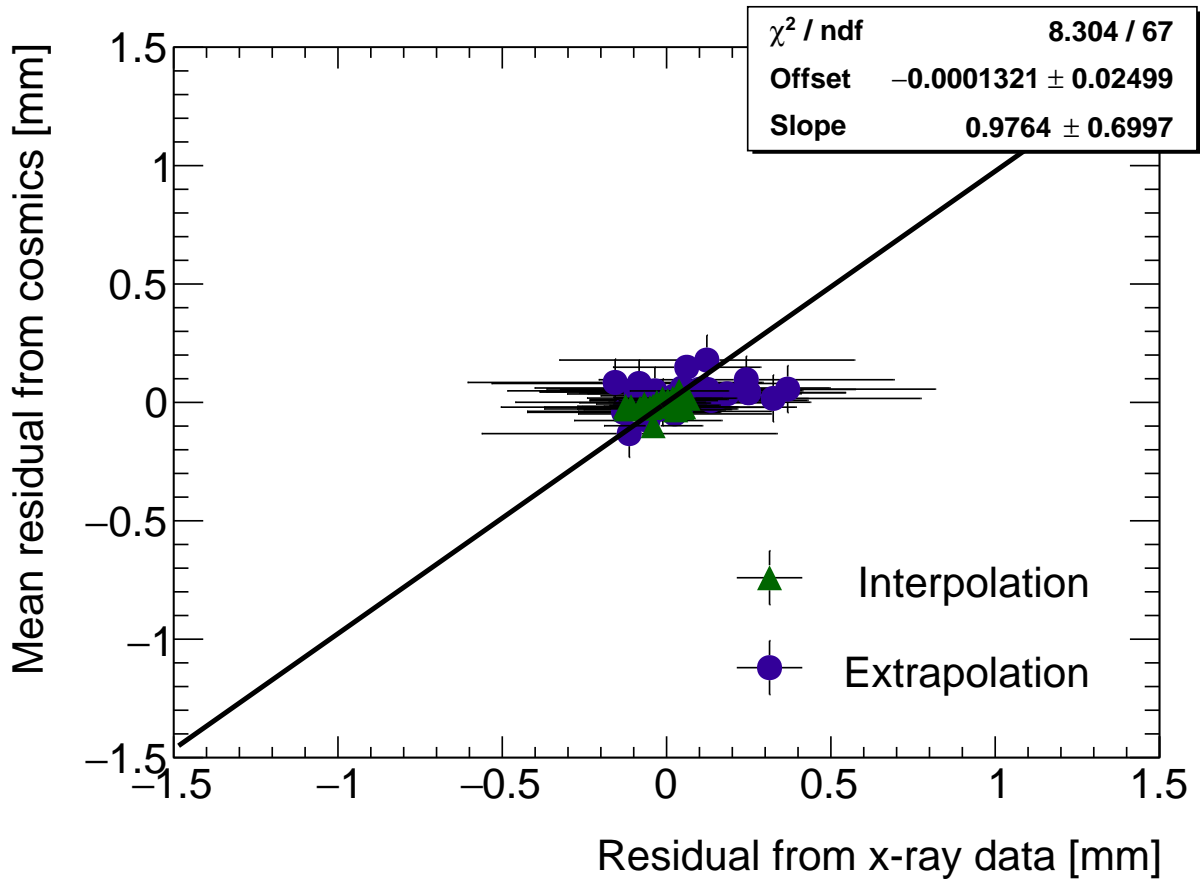


Figure D.2: Correlation plot between x-ray and cosmics residuals for all tracking combinations for QL2.P.8. Each rectangle is centered on an x-ray and mean cosmics residual pair. The width of the rectangles in  $x$  and  $y$  are the uncertainty in the x-ray and mean cosmics residual respectively. This is a printable version of figure 7.3 in section 7.1.